MOLECULAR DYNAMICS SIMULATIONS OF THE MECHANICAL DEFORMATION OF NANOPOROUS GOLD

by

Ashutosh Giri

B.S. in Physics, Adelphi University, 2010

Submitted to the Graduate Faculty of

Swanson School of Engineering in partial fulfillment

of the requirements for the degree of

Master of Science in Mechanical Engineering

University of Pittsburgh

2012

UNIVERSITY OF PITTSBURGH

SWANSON SCHOOL OF ENGINEERING

This thesis was presented

by

Ashutosh Giri

It was defended on

April 2, 2012

and approved by

Dr. Albert C. To, Ph.D., Assistant Professor, Department of Mechanical Engineering
and Materials Science

Dr. William S. Slaughter, Ph.D., Associate Professor, Department of Mechanical Engineering
and Materials Science

Dr. Patrick J. Smolinski, Ph.D., Associate Professor, Department of Mechanical Engineering
and Materials Science

Thesis Advisor: Dr. Albert C. To, Ph.D., Assistant Professor

MOLECULAR DYNAMICS SIMULATIONS OF THE MECHANICAL DEFORMATION OF NANOPOROUS GOLD

Ashutosh Giri, M.S.

University of Pittsburgh, 2012

Nanoporous (np) materials are a class of high strength and low density materials that have unique mechanical, chemical and physical characteristics that accompany them due to the size effect and high surface-area to volume ratio. Their mechanical properties play a vital role in many of their applications such as actuators, sensors and energy absorbers. In this work, the mechanical deformation behavior of np-Au under tensile and compressive stresses was studied by molecular dynamics simulations. The models representing np-Au were generated to capture the morphological features of np metals that have been processed via dealloying techniques. From the results of the simulations, it was found that these materials are brittle under uniaxial tensile loading and are very ductile under compressive loading. The engineering stress-strain relationship suggests that they have characteristic high yield strength and that these unique materials may even be stronger than bulk Au and also have the advantage of being highly porous. The macroscopic brittleness of np-Au presents a problem for useful application of these materials, but the microstructural features can be tailored to reduce the catastrophic failure. Under compression, their deformation behavior is similar to that of the Gibson and Ashby cubic unit cell model where cell wall bending is predicted to be the main deformation mechanism. One important difference between the predicted behavior according to the Gibson and Ashby model and the behavior observed from the atomistic simulations is that for the latter there is considerable strain hardening before foam densification occurs. By examining the

crystallographic defects, the strain hardening behavior has been attributed to defects in the crystal structure that accumulates at the joints.

TABLE OF CONTENTS

LIST OF TABLES

LIST OF FIGURES

PREFACE

I would like to thank my research advisor, Dr. Albert C. To for giving me the opportunity to work with him on this project. His guidance on academic and personal level throughout my graduate career is much appreciated. I would also like to thank Dr. William S. Slaughter and Dr. Patrick Smolinski for being on the committee and providing with useful suggestions for the thesis. In addition, I would also like to thank the computational nanomechanics group at the University of Pittsburgh for help throughout the project.

1.0 INTRODUCTION

In the field of nanotechnology, nanomaterials with morphological features on the nanoscale have caught the interest of researchers all around the globe. One class of these materials which are known as nanoporous (np) metals has attracted much attention in the recent years. The motivation behind the study of this class of materials arises from their unique mechanical, chemical and physical characteristics that accompany them due to the size effect and high surface-area to volume ratio. So far, these materials have been applied as actuators, sensors, insulators, electrodes, energy absorbents and also in areas of adsorption separation. [1-7] Furthermore, due to their high porosity or low relative density ($\leq 30\%$), they can be considered for usage as light-weight materials. Their mechanical properties play a vital role in many of these applications. For example, as actuators, np materials need to possess long term stability to withstand coarsening and sintering [7]. Therefore, studying the mechanical properties of these materials is important in better understanding their capabilities for various applications.

Np foams are a class of low relative-density materials with complex morphology and the study of their mechanical properties is still in its infancy. On the other hand, macroporous (mp) or cellular solids with pore/cell sizes greater than 1 µm have been studied extensively. Scaling equations that define the mechanical properties such as the yield strength and elastic modulus have been derived from vast amount of experimental results. These results point out the fact that the single most important feature that dictates the mechanical properties is the relative density

ρ^*/ρ_s of foams; which is the density of the cellular material, ρ^* divided by the density of the solid that makes up the ligaments, ρ_s. The size of the ligaments and the size of the pores/cells do not affect the mechanical properties of mp foams but for np foams with ligaments and pore sizes in the submicron regime, the combined effect of free surfaces and length scale effects cannot be overlooked. Many studies have tried to probe deeper into the effect of this microstructural length scale on the behavior of np foams but so far there has been no universal consensus on the deformation mechanisms involved. Some studies determine the measured value of the yield strength to be very high (greater than the yield strength of bulk Au) whereas the results from others do not support this high yield strength. Furthermore, contrasting results for the measured value of the elastic modulus from different studies adds more obscurity to the knowledge of their mechanical properties. In this thesis, the experimental and theoretical studies that have been dedicated to finding the length scale effects on the mechanical behavior of these novel materials will be reviewed and the results from our molecular dynamics (MD) simulations will be presented to shed more light on this topic.

Np materials are mechanically tested under different experimental techniques such as nanoindentation [8-10], beam bending [11, 12] and micro column compression tests [10]. Almost all of these studies have utilized the technique known as dealloying to synthesize np metal foams. In recent years, np foams have been processed as 1D nanowires, [13] 2D thin films, [14] and 3D macroscopic samples [15]. 2D Thin films of np gold (np-Au) have been processed by using commercially available white-gold leaves. These thin films are usually used for photonic applications because of their very well-defined microstructure with long-range order. In contrast, three-dimensional structures possess very disordered network of ligaments and the morphology can be best described as being “sponge-like”.

In metallurgy, dealloying is described as the removal of the less noble constituent from an alloy generally by dissolving it in a corrosive environment. [41] Usually, a binary alloy such as $Au_{25}Ag_{75}$ is placed under chemical or electrochemical dissolution and the result is a bicontinuous metal/void structure of the nobler element that is left behind. The ligaments are pure metal (Au) and the pores are interconnected and open.

Sieradzki and Newman [16] were the first to describe the dealloying process and since then considerable improvement has been made to synthesize np materials with controlled ligament and pore size. Specifically, the formation of np gold (np-Au) by this technique has been studied extensively [6, 13-15, 17-19] but the process is not just limited to np-Au, as alloys such as MnCu are used to form np copper [20].

The reason why np-Au is studied for length scale effects is because of the controllability of the pore and ligament size from 3nm to several micrometers in length [8]. This can be done via different methods: by controlling the initial alloy composition, changing the time for the dealloying process or annealing at different temperatures. Adjusting these factors in the synthesis of np foams produces varying pore and ligament size. This technique has a further advantage of being able to preserve the ligament and pore shape while not having an influence on the relative density of the np foams [7, 55]. Therefore, the study of size effects on the mechanical properties can be carried out while keeping the relative density of the np foam constant.

The microstructure resulting from the processing techniques is in the submicron length scale where free surfaces and interfaces have pronounced effects on plasticity of the material [47]. These effects depend on what type of material makes up the ligaments of the foams and the characteristic length scale associated with its plastic deformation [8]. As discussed earlier, the ligaments and pore sizes of np materials are in the nanometer length scale and their material properties can no longer be described by the bulk properties because of the presence of free surfaces. For the same reason, their mechanical behavior cannot be predicted by considering the behavior of mp foams. While this is expected, it is still helpful to compare the mechanical properties of these two classes of foams as there have been a lot of studies dedicated to mp foams. The mechanical properties of mp solids, such as the Young's modulus and yield strength have been predicted for metals, polymers, ceramics and glass [21]. Therefore, it is instructive to understand the basic mechanisms of foams before going any further on understanding the mechanisms of deformation in np foams.

1.1 THEORETICAL AND SEMI-EMPIRICAL FORMULA FOR MACROPOROUS FOAMS

In general, foams are three dimensional arrays of cells that form a network of interconnected struts and/or plates. They can be considered as cells enclosed by faces that are surrounded by edges. These edges join together to form vertices. Depending on how the cell material is distributed among the cell edges or cell faces, they can be categorized into open cell (empty cell faces) or closed cell foams (covered by plates or membranes). Their material properties depend on the material that constitutes the foam, its relative density, whether its cells are open or closed, and the mean cell diameter [21]. The discussion will be limited to open cell foams under compressive stress in this section. A thorough exploration of experimental as well as theoretical work in the study of mp materials can be found in the book "Cellular Solids" by Gibson and Ashby [21].

Efforts to model mp foams have been numerous and one of the ways is to use repetitive unit cell models that provide the homogenized behavior of foams based on these ideal unit cells. Most of the micromechanical models are limited to describing just the initial elastic constants: Young's Modulus E*, the shear modulus G*, and the Poisson's ratio ϑ* for the foams. They assume a cellular microstructure and use elementary strength of materials to describe the elastic constants by considering the ligaments as structural beams. These unit cells can be cubic [21], tetrahedral [22], tetrakaidecahedral [23] or bubble models [24]. The Gibson and Ashby cubic unit cell model shown in Figure 1 is the most widely used model and is used to describe the mechanical properties of mp foams.

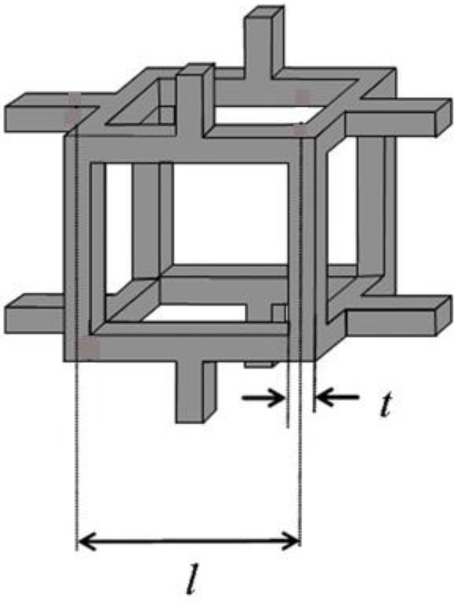

Figure 1: Schematic cubic unit cell model for mp foams.

The scaling relations that describes the yield strength (σ) and the young's modulus (*E*) of open cell foams in this model are given as:

$$\frac{E^*}{E_S} = C_1\left(\frac{\rho^*}{\rho_S}\right)^2 \tag{1.1}$$

$$\frac{\sigma^*{}_{pl}}{\sigma_{ys}} = C_2\left(\frac{\rho^*}{\rho_S}\right)^{3/2} \tag{1.2}$$

where the ρ^* is the density of the foam, ρ_s is the density of the bulk solid, E^* is the Young's modulus for the foam, E_s is the Young's modulus of the solid, σ^*_{pl} is the plastic yield strength of the foam, σ_{ys} and is the plastic yield strength of the solid.

The most important parameter that controls the mechanical properties of mp foams as can be inferred from Eqs. (1.1) and (1.2) is the relative density of the foam. Generally, the decrease in density implies the decrease in mechanical properties like stiffness, strength, and even ductility [17, 25]. The equations are fitted to experimental data and values for C_1 and C_2 are determined to be 1 and 0.3 respectively [21]. It is important to note that these equations only hold for low relative density foams. At low relative densities, open cells foams deform primarily by cell-wall bending [22, 26] and when the relative density increases the cell walls are extended or compressed which influences the mechanical properties [21]. Gibson and Ashby made corrections to Eq. (1.2) to get an equation that describes the behavior for foams with higher relative density given as:

$$\frac{\sigma^*{}_{pl}}{\sigma_{ys}} = C_2\left(\frac{\rho^*}{\rho_S}\right)^{3/2}\left(1+\left(\frac{\rho^*}{\rho_S}\right)^{\frac{1}{2}}\right) \tag{1.3}$$

Typically, under compressive stress, foams show three distinct stages of deformation as shown in Figure 2. For metal foams, the first stage of the stress-strain curve shows a linear elastic region that is controlled by cell wall bending. The slope of the stress strain curve at this stage gives the Young's modulus (E*) of the foam. The second stage is the long plateau in the stress strain curve where the cells collapse. The third and the final stage is where the stress rises abruptly and the foam densifies. This densification stage is marked by the complete collapse of cells which leads to the opposing cell walls touching each-other. The slope of the stress-strain curve at this stage is equal to the Young's modulus of the solid.

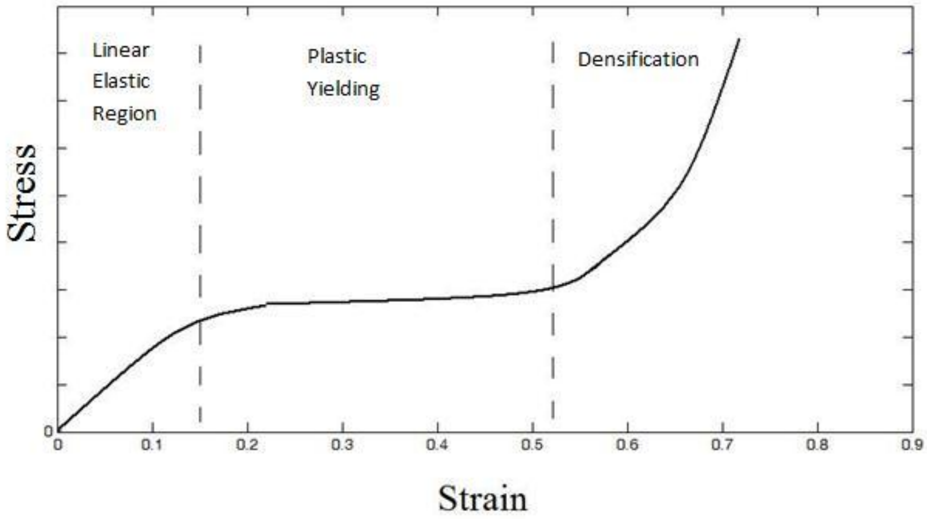

Figure 2: Representative compressive stress-strain behavior for metal foams showing linear elastic, plastic and densification stages.

1.2 EXPERIMENTAL STUDIES ON NANOPOROUS FOAMS

The study of mechanical properties of open cell np materials is important for the material's practical applications such as actuators and sensors where the mechanical stability is a prerequisite. The yield strength and elastic modulus of these unique materials have been reported by many experimental studies and the values range from 11MPa to 240MPa and 3GPa to 40GPa, respectively [9, 10, 20, 27-31]. The yield strength of bulk Au which depends on the sample history ranges from 10MPa to 200MPa [32]. Comparing the values of yield strength it is observed that np-Au may be stronger than bulk Au which would potentially open the door to a new class of high strength materials.

Np materials behave in a totally different manner than their bulk counterparts. For instance, even if the fully dense forms of Au behave in a ductile manner to mechanical deformations, the np forms have brittle characteristics under tensile force. They also show characteristics that are unique to porous materials under compressive and tensile loading. However, studies have shown that the scaling Eqs. (1.1) and (1.2) that predict the yield strength and Young's modulus for porous materials cannot be applied to np materials.

By plotting the experimentally measured Young's modulus or yield strength versus the relative density for different materials with varying relative density, Gibson and Ashby derived Eqs. (1.1) and (1.2) which is applicable to all kinds of open cell mp foams regardless of the material which they are made up of. One of the most frequently used experimental techniques to evaluate the yield strength of cellular solids is indentation tests. For np metal foams, nano-indentation is used to assess the hardness *H*. Conventionally for fully dense solids, the results of the indentation tests relate the yield strength to the hardness value as $H \sim 3\sigma$ [33]. However, for low density/high porosity foams (ρ^*/ρ_s >30%) it is assumed that the hardness *H* is related to the yield strength by $H \sim \sigma$ [9]. When a foam is compressed by an indenter, the cells beneath the indenter collapse in the direction of the punch and do not expand sideways (effective Poisson's ratio ~0). The relationship $H \sim \sigma$ also applies for nanoindentation tests on np foams and it is implied as well as experimentally proven that the material will not be constrained by its surroundings, making the effective Poisson's ratio ~ 0.

The first experimental study of deformation in np materials was reported by Rong Li and K. Sieradzki where they studied the fracture of this sometimes very delicate material. They were able to show that the ligaments do not become inherently brittle as the size of the ligaments became smaller [34]. Similarly, Khang *et al.* had previously shown that the ductile-brittle transition that takes place in random porous structures depends on the ratio of the sample size to the distribution of element strength. For their study of the fracture behavior of porous structures, Li and Sieradzki chose “highly porous Au” (np-Au) which they predicted would serve as a model system for future studies on different physical properties.

From then on, the mechanical properties of np-Au have been studied under different techniques as discussed previously. The bulk of the studies have relied on the technique of nanoindentation to measure the mechanical properties such as the yield strength and Young’s modulus. We will first review the elastic behavior of np Au under compressive loading. Then we will summarize the experimental results on their plastic behavior through nanoindentation tests followed by a discussion of results based on other techniques and then we will review the tensile properties of these unique materials.

1.2.1 Elastic modulus of nanoporous metals

The elastic modulus of nanoscale materials is not expected to increase with the decrease in the sample or the microstructural size [35]. Volkert *et al*. conducted uniaxial compression tests on np Au microcolumns with different diameters to study the effect of sample size on the Young’s modulus. From the unloading segment of their true stress-true strain curve, they obtained a Young’s modulus of 7 GPa under small plastic strains [30]. Likewise, the compression test on np-Au by depth sensing nanoindentation carried out by Biener *et al*. [10] also predicted the elastic modulus to be in the same order of magnitude. The experimental results can be compared with the analytical prediction made in Eq. (1.1) by substituting the Young’s modulus of single crystal Au (57-85 GPa) [36] and using a relative density of 36% (porosity of 64%). The scaling equation predicts the elastic modulus of np-Au foams to be approximately between 7 - 11 GPa which is in good agreement with the experimental results from Refs. [10] and [30]. It should be noted that these experimental studies did not observe a size effect on the measured Young's modulus value.

In contrast to the results from Refs. [30] and [10], Hodge *et al*. [37] showed that their experimental Young's modulus values for foams with relative density 25 to 41% was larger than what was predicted by the scaling equation with a density exponent $n=2$. They state that this difference is primarily due to the fact that the Gibson and Ashby relationship holds for low density foams with pore sizes greater than ligament sizes. However, with relative densities of 25-41%, the cell sizes as well as the ligaments are similar and contributions from ligament compression and extension cannot be ignored [37].

Mathur and Erlebacher [38] on the other hand have shown that the microstructural length scale affects the Young's modulus of the whole np structure. They showed that the Young's modulus of np-Au raises 4 folds when the ligament size decreases from 12nm to 3 nm. They performed mechanical testing on stress-free np-Au films with ligaments sizes on the range of 3nm to 40 nm using a buckling-based method [39]. Their results showed a dramatic rise in the values below 10nm ligament size but for larger ligaments, the size dependence was not as pronounced as for ligament sizes smaller than 10nm. For ligaments >12nm the np-Au ligament modulus compares well with values measured by nanoindentation tests and the values predicted by the Gibson and Ashby scaling relation in Eq. (1.1). The stiffening behavior, evident from the four-fold increase in the Young's modulus of np-Au films with ligaments smaller than 10nm, was attributed to various factors such as surface stresses. Another explanation was based on the structure of np-Au thin films where smaller ligaments results in a greater number of ligaments than coarse np-Au thin films with larger ligaments. This leads to a greater bending stiffness due to higher moment of inertia of the np structure as a whole. These findings are contradictory to the experimental results which conclude that the elastic properties are not dramatically influenced by length scale effects [35]. An example of such an experimental study can be found in Ref. [40] where the elastic modulus of Au nanowires (that resemble the ligaments in np-Au) as well as bulk Au has been shown to be independent of their diameter.

In addition to researches on the size effects, the effect of residual Ag content on the elastic modulus of np-Au foams was studied in Ref. [37]. It is reported that dealloying of Au-Ag alloy which requires suppressing surface diffusion to produce ligaments smaller than 30 nm tends to yield higher concentrations of residual silver content. This increases the density of the structure which in effect increases the Young’s modulus of np-Au. This can be inferred from the scaling relation in Eq. (1.1) which predicts that increasing the relative density will increase the Young’s modulus of any generic foam. In this context, the strong elastic length scale effects below 12nm ligament size as seen in Mathur and Erlebacher’s study could be explained due to the presence of residual Ag.

1.2.2 Yield strength of nanoporous metals.

As discussed earlier, the use of indentation has been shown to be a valid technique to measure the yield strength of mp foams. Issues such as indentation size effects and densification effects have to be addressed to validate this technique. In the case of densification effects, both for np and mp foams, the area underneath the indenter have been shown to compress and densify, whereas the area outside the indentation diameter remains intact [10, 41]. Andrews *et al*. [41] addressed the indentation size effects by performing indentation tests on mp aluminum open cell foams. The effect of specimen size relative to the cell size on the mechanical properties was investigated in their study and the results showed an exponential decay in hardness as a function of the normalized indenter size as well as cell size. In the case of np materials, Hodge *et al*. [42] were successful in showing similar effects for np-Au. The work done by Andrews *et al*. [41] also showed that for low density foams, the yield strength values from compression tests and indentation tests are similar. Similarly, Chen *et al*. [25] validated the nanoindentation technique by comparing the experimental results from nanoindentation with the results from bulge test measurements and finite element analysis on the mechanical behavior of thin np polymer films and showing that the values obtained matched well.

One of the significant findings of the nanoindentation tests performed on np foams with high porosity is the characteristic high strength. Biener *et al*. [9] have measured the hardness value of np-Au with 42% relative density and 100 nm ligament length to be approximately 10 times higher than the hardness value predicted by the Gibson and Ashby scaling equation. Through SEM micrograph images of the np structure, they were able to observe that the dominant deformation mechanism during nanoindentation test on np-Au was ductile, i.e. plastic densification.

Similarly, Volkert *et al*. [30] showed that the yield strength of 15 nm ligaments in np-Au approaches the intrinsic strength of gold. The experimentally determined hardness value of 100 MPa was replaced in the scaling relation in Eq. (1.2) with a relative density of 36% and a value of 1.5 GPa was predicted for the yield stress of individual ligaments in the np-Au structure. This prediction compares well with the expected theoretical shear strength of Au at which the atoms on adjacent atomic planes slide past one another without the influence of dislocations.

Apart from their surprisingly high yield strength, a relatively more expected result from the nanoindentation tests is the size effects that influence the mechanical behavior of np foams.

In recent years, it has been shown extensively that the sample size and grain size affect the plastic behavior of nanostructured materials in general. Both experimental studies and molecular dynamics (MD) simulations suggest that the mechanical behavior of materials at the submicron length scale is strongly influenced by what is called the size effect. Hodge *et al*. [42] studied the microstructural length dependence on the yield strength via a series of nanoindentation tests performed on np-Au foams with relative densities ranging from 20% to 42%. They compared the experimental values with the values obtained from the Gibson and Ashby scaling equation. It was found that a decrease in the ligament size was accompanied by a decrease in the yield strength of np-Au foams at the same relative density. This stands as a contrast to the results of studies on macrocellular foams (ligament size greater than 1.0 µm) and the predictions made by Gibson and Ashby scaling relation which do not incorporate a length scale dependence of mechanical behavior on the ligament size given for a fixed porosity. Once the ligament size approaches 1.0 µm, the experimental results of the nanoindentation tests matched well with the scaling relationship.

Similar to these results, Mabuchi *et al*. also studied the effect of ligament size on the yield stress via nanoindentation tests on np-Au specimens fabricated by dealloying [43]. By plotting the yield stress against the size of Au ligaments they were able to come up with the relationship,

$$\sigma_{ys} = Kd^{m} \tag{1.4}$$

where d is the ligament size, K is a constant and m is the ligament size dependence. From the plot, the value of m in Eq. (1.4) was found to be -0.20. This value was comparable to literature values of m in similar equations for face-centered cubic metallic nanowires [40, 44] suggesting that the deformation mechanisms involved are similar in both cases. Mabuchi *et al*. [43] sate that the mechanisms involved in FCC metallic nanowires such as the reduction in number of defects in grains due to size effects, the repression of emission and reabsorption of dislocations and dislocation nucleation at free surfaces may be the likely mechanisms involved in length scale effects seen in np-Au as well.

In the context of deformation mechanisms, there has been no consensus on the issue of which mechanisms govern the length scale dependent deformation in np gold or even in columns and nanowires of gold. However, studies have tried to compare the deformation behavior of the ligaments in np-Au, to that in columns and nanowires of Au. In Refs. [8] and [27], results were analyzed for indentation tests on np-Au as well as for nanomechanical measurements performed on submicron Au columns and nanowires. As in np-Au, the scale dependent high yield strength is also observed for the Au micropillars/nanowires. Indeed, microcolumns and nanowires that have small single crystals show very high strength values. Furthermore, Geer and Nix [33] showed that the yield strength of submicron Au columns also follow the size dependent characteristics observed in np-Au and that the theoretical yield strength can be achieved when the size of the diameter of Au columns decreases down to a few hundred nanometers. Volkert and Lilleodden [30] performed nanoindentation tests on Au micropillars that were machined in the surface of a large grained Au sheet using a focused Ga^+ beam. The results for their measured yield strength were shown to follow the power law d^{-n} where d is the column diameter and n is 0.61. These results match well with the relationship of yield strength and ligament size as in Eq. (1.4) for np-Au suggesting that the same deformation mechanisms are involved in ligaments of np-Au and Au micropillars.

The size effect observed for nanostructures has been explained by the presence of free surfaces at the nano-scale that limits the number of dislocation sources. Beiner *et al.* [10] state that the microcolumns of Au can be related to the ligaments in np-Au where the applied stress needed to activate the dislocation sources increases until the theoretical shear strength is reached as the size of the ligaments decreases. Their size dependence observed for np-Au is in excellent agreement with the results from microcompression tests on sub-micron Au columns. The higher than expected source activation stress is because of various factors such as changes in active source size, internal stress fields or number of sources [30]. This explanation matches well with most of the studies on np-Au which have shown that the yield strength in ligaments approaches the theoretical shear strength.

In contrast to the possibility of similar deformation mechanisms involved in np-Au and Au microcolumns/nanowires, Ref. [27] has shown that the deformation mechanisms may be different in the two cases. They studied the micromechanisms of deformation in np-Au nanowires through transmission electron microscope (TEM) investigation of the deformed structure after indentation. It is shown that the use of np-Au nanowires instead of 3D macroscopic samples does not influence the results because the mechanisms observed in np-Au nanowires are similar to that in bulk np-Au with similar ligament sizes. Gibson and Ashby had proposed that the plastic collapse of mp foams occur through bending caused by localized plastic deformation of hinges at the nodes [21]. TEM images from Ref. [27] show clearly defined surface steps which indicate that plastic deformation occurs in a localized fashion through bending of the ligaments, similar to the conclusions of Gibson and Ashby. Furthermore, high densities of Shockley partial dislocations and microtwins were mostly found to be located around the nodes where the ligaments form junctions. They did not find perfect dislocations in the ligaments of deformed np-Au nanowires, consistent with mechanisms-based strengthening models on strain gradient hardening [45]. Strain gradient models are continuum models which state that there are geometrically necessary deformations that obstruct further deformation and also have a strengthening effect on the material. Their TEM images showed that the Shockley partial dislocations propagate and interact with each other to generate twins and complex microtwinned structures. They propose that the fundamental distinction in compression between nanowires and np-Au nanowires is that for the np structure, the principle deformation mode is bending.

In another experimental study, Sun *et al.* [46] took the advantage of recently developed in-situ nanoindentation technique and studied 150nm thick np-Au thin films with ligament width ranging from 10-20nm. The deformation of microstructure was studied through TEM investigations during the nanoindentation process. From the TEM images, they deduced that during the initial stages of nanoindentation, where np-Au was observed to deform easily, the outermost layer of ligaments was compacted by the indenter while the rest of the underlying structure remained undeformed. Progressively, upon further indentation, the compaction front moved ahead of the indenter and neighboring ligaments collapsed. Their load displacement curve showed local maxima at two different points in the loading curve that was separated by roughly the size of the pores. They attributed this result to the collective collapse of a layer of pores where ligaments buckle simultaneously causing a decrease in the indenter load. Also, the dislocations that arose initially due to indentation were traced by the TEM images and were shown to span the width of the ligament. These dislocations moved easily in the ligaments and underwent sequential glide to the ligament nodes, where it was observed that they sometimes tangled with dislocations from other ligaments.

Unlike the vast amounts of studies that report the length scale effects and the high yield strength values, there have been but a few studies that have reported on the strain hardening behavior of np-Au. This may be due to the fact that majority of the experimental studies utilize nanoindentation technique to extract load/displacement record which although is an easier technique compared to other mechanical testing methods, a complex strain history occurs that makes it very hard to show the strain hardening behavior of np-Au. From the study conducted by Volkert *et al.* [30], the true stress-strain relationship obtained by uniaxial compression showed considerable strain hardening (approximately two times the yield strength) up to 30% strain and a plastic flow stress was expected to follow after that strain. Ref. [27] has also reported on the strain hardening behavior from nanoindentation testing of np-Au but as thin nanowires instead of 3D macroscopic samples. They explained that the strain hardening behavior is a result of contact between ligaments even at low strains due to higher relative density of the foams.

Another useful and less complex experimental procedure compared to nanoindentation test is the pillar micro-compression test to measure the yield strength of np-Au. Biener *et al.* [10] have carried out uniaxial compression tests on micrometer-sized np-Au columns through the technique developed by Uchic *et al.* [47]. The columns were machined by the focused ion beam technique and the height-to-diameter ratio was approximately 2. In their study, no evidence of strain hardening can be found from the true stress- strain curve that shows a constant plastic flow stress after approximately 2.5% strain. The high yield strength values observed from nanoindentation tests were also observed in this compression test, indicating that the testing method is not responsible for the surprisingly high yield strength of np-Au.

In contrast to the high yield strength of np-Au found by studies discussed in the above paragraphs, there have been studies that have reported significantly different values for the yield strength. Ref. [48] reported the yield strength to be an order lower in magnitude when compared with the values obtained by the nanoindentation experiments on np-Au. Their np-Au samples being tested were fabricated through a different method introduced by Jin *et al.* [28]. Generally, np-Au fabricated through the process of dealloying has undesirable material failures such as stress corrosion cracking and brittle cracks that develop due to shrinkage of the volume [18]. However, Jin *et al.* [28] were able to produce samples of np-Au that were free of cracks. The shrinkage during dealloying was less than 2% in volume for their samples and crack formation during synthesis was thus avoided. They report the results of compression tests carried out on a testing machine that shows excellent ductility with nearly the full density of the samples being compressed without fracture. Electron backscatter diffraction (EBSD) maps showed homogeneous plastic deformation in contrast to the more conventional observation of deformation bands forming and propagating through the sample. The low yield strength values measured from this experiment differs from the high strength values of previously reported indentation tests where the hardness data was reported by equating the hardness to the yield strength ($H \sim \sigma$) which is only true for low density foams. Another reason for the vast difference in the results may be because the np-Au fabricated by their method has a long-range coherent crystal lattice where each grain consists of billions of nanoligaments with a common set of crystallographic slip planes [28]. Their EBSD maps showed conservation of the grain structure throughout the deformation process suggesting that ligaments collectively shear along common planes and directions in contrast to collapsing as in conventional low-density foams. Previous studies have related the macroscopic strength to be governed by the combination of relative density and the size dependence of the ligaments whereas in their study, they showed that the correlated deformation events of individual ligaments also have to be accounted for.

1.2.3 Tensile response of nanoporous metals

There has been fewer reports on the fracture behavior in tension of np-Au compared to the number of reports on their compressive behavior. Earlier studies on the stress corrosion cracking of Ag-Au alloys also reported brittle failure under corrosive environment [17, 34, 49]. These studies support the film-induced cleavage model, where the formation of a thin layer of np gold (from dealloying) initiates a crack that propagates through the dealloyed layer and into the bulk material (which is not corroded). As stated earlier, even though bulk Au show ductile deformation behavior, it has been found that np-Au are macroscopically very brittle, which makes the handling of these specimen very difficult. Li and Sieradzki [34] showed that samples that are significantly larger compared to their microstructural pore/ligament size tend to be more brittle. This characteristic makes the mechanical testing of these specimens under tensile loading very difficult to conduct.

It has been observed that there is considerable volume shrinkage and tensile built stress during the dealloying process of np-Au [18]. The increase in Ag content of the Ag-Au alloy used for dealloying also increases the brittleness of the structure. This is seen in the samples of $Ag_{80}Au_{20}$ alloys which disintegrate due to tensile stress buildup during dealloying whereas samples from $Ag_{70}Au_{30}$ alloys do not disintegrate. However, np-Au nanowires have been synthesized from $Ag_{82}Au_{18}$ alloys which leads to an important deduction made in Ref. [18] that nanowires and also thin films can accommodate this tensile built stresses better than 3D macroscopic samples as they are less susceptible to shrinkage.

A detailed study of the fracture behavior of np-Au using a three-point bending configuration was carried out by Biener *et al*. [11]. The samples were shown to fail on the tension side rather than on the compression side (stronger in compression) through crack propagation that lead to a catastrophic failure of the np-Au structure. There was no macroscopically visible plastic deformation prior to failure indicating that the material fails through brittle crack propagation. Further SEM images of the microstructure revealed a characteristic necking feature of individual ligaments that show ductile failure due to overloading. As in the MD simulations of Au nanowires [50], the ligaments showed as much as 100% elongations. Gold, being the most malleable metal, the ductility shown by ligaments of np-Au is as expected.

The macroscopic brittleness on the other hand is said to be the consequence of narrow ligament-strength distribution. In an earlier study, Khang *et al*. [51] also came to a similar conclusion for a random fuse network model. According to this explanation, the rupture of the weakest ligament starts the crack propagation through the network structure by stretching and overloading adjacent ligaments. The crack follows the path of least resistance through the np-Au structure. Thus, the overall strength of the network structure is given by the largest critical defect that causes the highest stress concentration. In Ref. [11], it was shown that the grain boundaries of the Ag-Au master alloy contained Ag enrichment that develops reduced density material during dealloying thus creating 2D like voids. These voids act as stress concentrations that nucleate the crack propagation. They state that by introducing a broader ligament strength distribution, the mechanical properties of np-Au can be improved.

Similar results for the fracture behavior of np-Au have also been observed in Ref. [48] where the samples were tested by a custom-built mechanical testing apparatus. Strain measurements were carried out through Digital Image Correlation [52] that enables non-contact strain measurement and has the advantage of full-field capability. Their tensile test specimens did not exhibit plasticity because of the macroscopic brittle nature of np-Au deformation. After the elastic response, a small crack was seen to propagate that ultimately stretched perpendicular to the tensile axis indicating brittle fracture. They also report on the ductile failure of the individual ligaments which can be observed in the SEM images. The deformation behavior is reported to be highly localized as the neighboring structure remains intact while plastic deformation of ligaments is confined to 1-2 ligaments which fall in the region of the crack surface. They attributed this phenomenon to the inability of the ligaments to store the dislocations that glide to the surface and escape.

2.0 A REVIEW OF MOLECULAR DYNAMICS

Molecular dynamics simulations provide the computational description of the trajectory of atoms in a system, which are used to estimate the equilibrium and dynamic properties of systems for which analytical solutions are impossible. The time evolution of a set of atoms or molecules at finite temperature is followed by integrating their equations of motion. These atoms or molecules are essentially treated as point masses that have no internal structure or degrees of freedom. The quantum nature of the atoms is neglected and they are modeled as classical particles that follow the Newton's equations of motion. The motion of the system of particles obeys the Newton's second law given as:

$$m_i \frac{d^2 \overset{\rightarrow}{r_i}}{dt^2} = \vec{F}_i \left(\overset{\rightarrow}{r_1}, \ldots, \overset{\rightarrow}{r_N} \right) \tag{2.1}$$

where m_i is the mass and $\overset{\rightarrow}{r_i}$ is the position vector of the i^{th} particle, N is the total number of particles and $\vec{F_i}$ is the force exerted on the i^{th} particle by possibly all other particles. As the forces only depend on the positions of the particles, the particles interact in a conservative force field. To capture the essential physics of the motion of particles, the potential energy between these particles has to be modeled accurately. The potential energy $U(\vec{r})$ is a function of each atom's position and the force on each atom can be calculated by taking the gradient of this potential energy.

$$\vec{F} = -\nabla U(\vec{r}) \tag{2.2}$$

It can be shown that the total energy of the system given by the equations of motion is conserved as it should be. Eq. (2.1) is a second order differential equation which becomes complicated to solve analytically when more than two particles interact with each other. This is the so called *many-body* problem. Thus the basic objective of MD simulation is the integration in time of the equations of motion. Given a set of initial positions and velocities of the particles, the position and velocity as a function of time of the N particles that constitutes the dynamical system is followed ($6N$ variables). The trajectory being calculated is in $6N$-dimensional phase space (of which $3N$ represents positions and $3N$ represents momenta) and the Newton's equation of motion will make the trajectories evolve in the phase space. MD uses time integration algorithms to integrate the Newton's equations of motions and these algorithms are based on *finite difference methods*, where time is discretized on a finite grid, the *time step* Δt being the distance between consecutive points on the grid [53]. Once we have the computational algorithm which allows us to evolve the system of particles in $6N$ phase space, we can calculate the thermodynamical properties or the ensemble averages of the system of atoms. Time average provides an estimate of ensemble average of physical properties over the system trajectory. For example, the average physical property X is given as:

$$\bar{A} = \frac{1}{T}\int_0^T A(t)\,dt \tag{2.3}$$

In this way, the physical properties of interest such as temperature and stress of the system can be calculated through MD simulations. The interatomic potential used for this work will be discussed in Section 2.1 and the numerical integration method will be discussed in Section 2.2.

One of the most significant limitations with MD simulations is the time scale problem. The dynamics involved in the motion of atoms is on the time scale of $\sim 10^{-15} s$. Whereas, macroscopic processes such as uniaxial compression tests usually take time scales in the order of seconds. This time scale barrier is impossible to breach with the current computational resources available. Integrating from the atomic motion to the dynamics of the mesoscale and the macroscale is an impossible task via MD.

2.1 EMBEDDED ATOM METHOD (EAM) POTENTIAL

In atomistic simulations, the use of the correct interatomic potential dictates the accuracy of the physics described by the simulation. Potentials that calculate the interaction of particles from the electronic structures are the most accurate methods to describe the atomic level physics but are also computationally very costly. *Ab-initio* MD or first principle MD have been developed from that basis but can only be implemented to study a system with a few number of atoms. Simpler interatomic potentials such as pair potentials have been developed to cut the computational cost by calculating the energy pairwise. However, these models fail to capture the essential physics such as the vacancy formation energy and surface relaxation in crystal structures with FCC metallic bonding. To account for this, various semi-empirical potential models have been proposed that fit the parameters to data from experimental or first priciple MD simulations.

The MD simulations performed in this work utilized one of the semi-empirical potential models called the embedded atom method (EAM) [54]. This interatomic potential dictates the interaction between atoms in the np-Au structures generated for this work. For the EAM potential, the total energy E of the system is given as:

$$E = \sum_{i}^{N} \left(F_i\left(\rho_i\right) + \frac{1}{2} \sum_{j \neq i}^{N} \phi_{ij}\left(R_{ij}\right) \right) \tag{2.4}$$

where N is the total number of atoms in the system. F_i is the embedding energy and ρ_i is the electron density at atom i while ϕ_{ij} is the pair potential and R_{ij} is the distance between atoms i and j. The embedding energy term F_i is the energy required to embed an atom into an electron density which comes from the other atoms.

2.2 VELOCITY-VERLET ALGORITHM

In this work, the velocity-verlet algorithm is used to numerically integrate the equations of motion. The integration determines the position and velocity of the particles at each timestep. The basic verlet algorithm was derived from the Taylor series expansions of the position $\vec{r}$ in both forward and backward in time t:

$$\vec{r}(t+\Delta t) = \vec{r}(t) + \vec{v}(t)\Delta t + \frac{1}{2}\vec{a}(t)\Delta t^2 + \frac{1}{6}\vec{b}(t)\Delta t^3 + O(\Delta t^4) \tag{2.5}$$

$$\vec{r}(t-\Delta t) = \vec{r}(t) - \vec{v}(t)\Delta t + \frac{1}{2}\vec{a}(t)\Delta t^2 - \frac{1}{6}\vec{b}(t)\Delta t^3 + O(\Delta t^4) \tag{2.6}$$

Combining equations and gives,

$$\vec{r}(t+\Delta t) = 2\vec{r}(t) - \vec{r}(t-\Delta t) + \vec{a}(t)\Delta t^2 + O(\Delta t^4) \tag{2.7}$$

where acceleration $\vec{a}(t)$ of the particle with mass m is given as:

$$\vec{a}(t) = -\frac{\nabla U(t)}{m} \tag{2.8}$$

The position of a particle forward in time by *Δt* is obtained from the knowledge of the current position, the previous position backward in time by *Δt* and the acceleration at the current time. The truncation error scales as $O(t^4)$ and the algorithm is stable. Even though the algorithm does not include the velocity of the particle to calculate the position of the particle, for thermodynamic outputs such as the temperature, the velocity of the particle has to be calculated by:

$$\vec{v}(t) = \frac{\vec{r}(t+\Delta t) - \vec{r}(t-\Delta t)}{2\Delta t} + O(\Delta t^2) \tag{2.9}$$

The order of accuracy associated with this equation is $O(t^2)$. To reduce the truncation error, a better algorithm called the velocity-verlet algorithm is used as the numerical integrator for the simulations performed in this work. The following steps are carried out to calculate both the position and velocity a full timestep forward in time:

- Calculate position,

$$\vec{r}(t+\Delta t) = \vec{r}(t) + \vec{v}(t)\Delta t + \frac{1}{2}\vec{a}(t)(\Delta t^2) \tag{2.10}$$

- Calculate velocity at half a timestep forward in time,

$$\vec{v}\left(t + \frac{\Delta t}{2}\right) = \vec{v}(t) + \frac{\vec{a}(t)\Delta t}{2} \tag{2.11}$$

- Calculate acceleration and velocity at the next timestep,

$$\vec{a}(t+\Delta t) = -\frac{\nabla U\left(\vec{r}\left(t+\Delta t\right)\right)}{m} \tag{2.12}$$

$$\vec{v}(t+\Delta t) = \vec{v}\left(t + \frac{\Delta t}{2}\right) + \frac{\vec{a}(t+\Delta t)\Delta t}{2} \tag{2.13}$$

3.0 METHODOLOGY

3.1 MODEL GENERATION

One of the main reasons why there have not been many computational studies conducted on np materials is because of their complex morphology, which makes modeling their microstructure very difficult. For general cellular structures, foam topology is typically disordered and non-uniform. To accurately model np structures, it is important to incorporate random cell/pore size and make their locations random in the structure, thus creating a non-uniform cell ordered in space. In addition to the randomness in the location of cells, the ligament cross-sections also have to be non-uniform. The open cell np structures in this study met all of these requirements and the model generation was based on the same method applied for modeling microcellular carbon foams as in Ref. [55]; by subtracting a series of randomly generated but interconnected spheres from an Au crystal block. The resulting structure is a sponge-like, porous system with randomly oriented and located ligaments.

The general idea behind creating the porous topology is deleting atoms that fall inside certain regions within a pristine solid block. These regions are defined by first interconnecting a "target sphere" with randomly chosen number of "neighbor spheres". The neighbor spheres then become the target sphere and each of these spheres is interconnected with its neighbor spheres. In this way, a network of interconnected spheres is generated as shown in Figure 3. Atoms that fall inside the regions defined by these spheres are deleted and what are left behind are atoms that form ligaments of the open celled np structure. One of the restrictions to follow when generating these spheres is that the neighbor spheres of the same target sphere cannot overlap each other. The distance between the centers of the two neighbor spheres can be adjusted by controlling the "non-overlapping ratio", which is defined as the ratio between the distance of two non-intersected spheres and sum of the radii of these two spheres. Another important parameter that influences the overall porosity of the structure is the "overlapping ratio" between a target sphere and one of its neighbors. This is defined as the ratio of the distance between the center of the two spheres and the sum of their radii. There can be 3 to 7 number of neighbor spheres that a target sphere can accommodate. However, we assign 5 neighbors to be the maximum for a target sphere. It is impossible to generate interconnected spheres with less than 3 neighbor spheres and likewise it is impossible to add more than 7 neighbor spheres on a target sphere due to the restriction that the neighbor spheres cannot overlap each other. By varying the adjustable parameters we create structures with varying porosities from 66% to 78%. This technique also allows the control of ligament width and joint size in the structure.

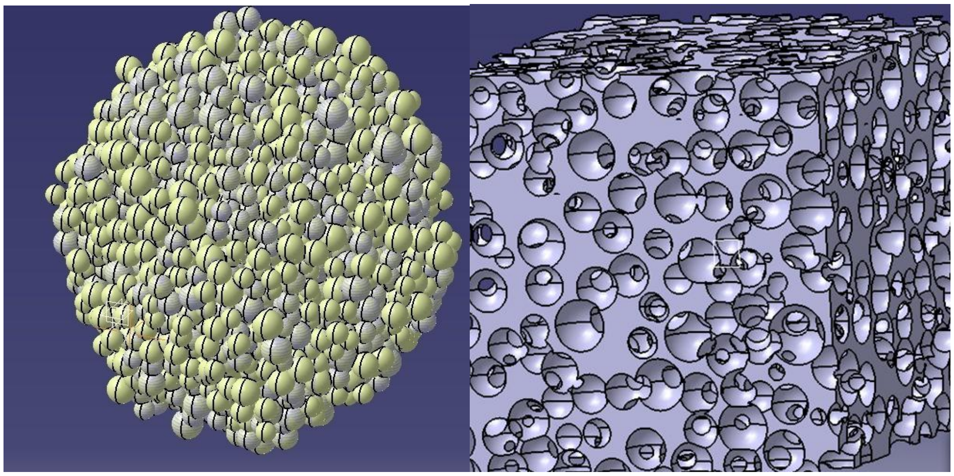

Figure 3: Generation of Random Nanoporous Structure. (a) 3,000 interconnected spheres generated. (b) Final porous structure after deleting the interconnected spheres from a solid block.

The first generated sphere is automatically considered as the first target, and then, 5 points are randomly picked on the surface of the first sphere. These five points represent the random points on the surface of 5 neighbor spheres of the corresponding target sphere. Radius of each of these neighbor spheres is than determined by the initial set-up value of the overlapping ratio. Centers for the neighbors are determined using the spherical coordinate representation of the sphere:

$$x = x_0 + r\sin(\theta)\cos(\varphi) \tag{3.1}$$

$$y = y_0 + r\sin(\theta)\sin(\varphi) \tag{3.2}$$

$$z = z_0 + r\cos(\theta) \tag{3.3}$$

where (x_0, y_0, z_0) is the central coordinates of the target sphere, (x, y, z) is the coordinate of the center point of a neighbor sphere, r is the distance between the center of target sphere and the center of the neighbor sphere, θ and φ are stochastic variables, which determine the position of the point on the spherical surface with radius r whose center coincides with that of the target sphere. φ is randomly chosen from 0 to $\pi/2$ and θ is randomly chosen from 0 to π.

If the spheres that intersect with the same target sphere also intersect with each other, or, the distance between these spheres is smaller than the initial prescribed value (usually controlled by "non-overlapping ratio" prescribed to be greater than 1.1), one of these two neighbors is discarded and a new neighbor is created until the constraints are satisfied. After the neighbors of the first target reach the maximum of the prescribed value of 5, a new target is randomly chosen among its neighbors. The first target sphere is automatically considered as one of the neighbors for the new target sphere. Then, the same scenario is applied to the new target sphere, and 4 more neighbor spheres are generated to intersect with that sphere. A total of 3000 spheres were generated in this process as shown in Figure 3a. The resulting porous structure after deleting the spheres from a solid block is shown in Figure 3b.

For np materials, as discussed in the previous section, the ligament size and joint size affect the overall mechanical properties of these materials. The algorithm used to generate the spheres allows us to adjust the size of ligaments and joints (that connect the ligaments) in order to study their relationship with the mechanical properties. After some tests, it has been found that the overlapping ratio and the radius of each sphere are the only two parameters that can significantly change the porosity as well as the widths of the ligaments and joints. The overlapping ratio of two interconnected spheres has a more significant effect on the porosity, while the radius for each generated sphere has a more significant effect on the ligament and joint widths. By varying the overlapping ratio, a series of structures with different porosities but similar range of pore sizes can be produced. Whereas, by varying the range of pore sizes, series of np structures with different pore sizes but similar porosity can be produced.

Though all the studies were conducted using random np structures, in order to study the effect of ligament size and joint width on the mechanical response, periodic np structure was generated and employed as shown in Figure 4. This is because it is much easier to extract individual ligaments and joints from the periodic np structures for further study than from the random np structures. Given the same porosity, the ligaments and joints in the periodic structure are identical and their size represents the average size in the corresponding random structure. Though the distribution of the ligament and joint sizes is lost in this procedure, it is enough to explain the underlying mechanism of the observed stress-strain behavior of the random np structures as will be discussed.

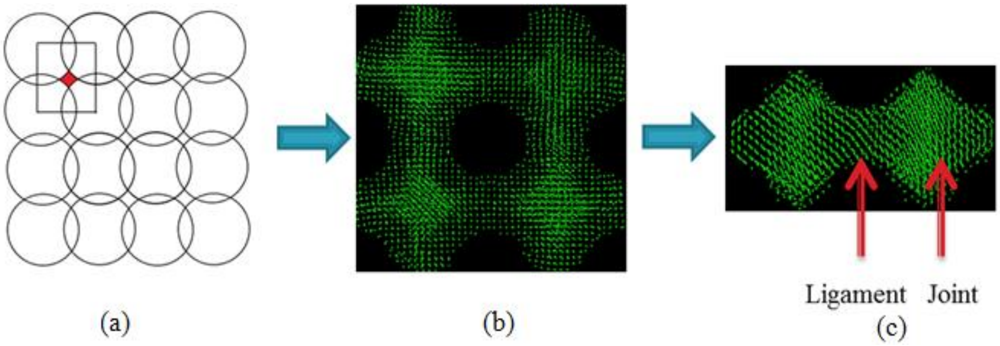

Figure 4: Generation of Ligament-joint Composite: (a): Imagined sphere matrix, the shaded area can be considered as the ligament cross-sectional area; (b): optimistic 3D mesh structure; (c): Final composite, ligament with 2 joints on each end.

The np periodic structures were generated by subtracting a periodic rectangular array of spheres from a solid aluminum block. The overlapping ratio was taken to be identical to that employed in the corresponding random np structure while the radius of the spheres was varied to produce the same porosity of the specific random structure. In the front view of a typical periodic structure shown in Figure 4(a), all the centers of 4 intersecting spheres share the same plane, and the lines connecting the centers of the four neighbors form a square. The shaded region in the middle is the cross section of a ligament in the np structure. As the cross-sectional area of ligaments and joints are close to a square, we approximated the widths for these microstructures by taking the square root of their cross-sectional area. Fig. 4(b) and 4(c) shows zoom-in views of the atomistic model of the periodic np structure.

3.2 SIMULATION DETAILS

Sandia National Labs' LAMMPS (Large-scale Atomic/Molecular Massively Parallel Simulator) code [56] was used to simulate tensile and compressive deformation of np-Au with different porosities. The structures were deformed under uniaxial strain at a uniform rate. Size effects have been shown to have large influence on the mechanical behavior of FCC metals [50]. Therefore, the dimensions of the model were selected to be at least ten times the length scale of the largest microstructural feature [63], which was the sphere diameter for the structures. Based on this criterion, a block size of $80 \times 80 \times 80$ CLU was used for all structures. At the start of each simulation, energy minimization was performed on all np structures and these structures were equilibrated for a total of 20 ps at a time step size of 0.5 fs at 300 K under the microcanonical (NVE) ensemble. The Langevin thermostat was applied to maintain the temperature at 300K throughout the simulations.

Engineering strain was used as the measure of deformation during the simulation. A strain rate of $1 \times 10^{8} s^{-1}$ was applied on the different porosity np-Au structures. Displacement boundary condition in the $\langle 100 \rangle$ crystallographic direction was applied on 2.5 CLUs at either end. Atoms in the region of the block that were constrained to the prescribed boundary conditions were not subjected to the equations of motion since their positions are manually updated, and so these atoms were used directly to calculate the forces for other atoms. The stress in the structure was calculated from the 'time averaged' forces on atoms under the displacement boundary condition at one end of the block in the direction of the applied strain. These forces were summed together and divided by the cross-sectional area of the np structure to obtain the 'time averaged' stress in the direction of the applied strain.

To visualize the local stress states of atoms, the von Mises stress for each atom was calculated and the details are discussed in Section 3.2.1. To visualize the defects such as partial dislocations and stacking faults, the centrosymmetry parameter was computed at different strain levels during the simulation and the details of the process are discussed in Section 3.2.2.

3.2.1 Symmetric per atom stress Tensor

LAMMPS has the feature to compute the per-atom stress tensor for a group or all of the atoms in the simulation. The stress tensor has 6 components that are stored as a vector in the following order: *xx*, *yy*, *zz*, *xy*, *xz*, *yz*, where *x*, *y* and *z* represent the three orthogonal directions in an Euclidean space. For an atom, the stress tensor is given as:

$$T_{\alpha\beta} = -\left[\begin{array}{l} mv_a v_b + \frac{1}{2}\sum_{n=1}^{N_p}(r_{1\alpha}F_{1\beta} + r_{2\beta}F_{2\beta}) + \frac{1}{2}\sum_{n=1}^{N_b}(r_{1\alpha}F_{1\beta} + r_{2\beta}F_{2\beta}) + \\ \frac{1}{3}\sum_{n=1}^{N_a}(r_{1\alpha}F_{1\beta} + r_{2\beta}F_{2\beta} + r_{3\beta}F_{3\beta}) + \frac{1}{4}\sum_{n=1}^{N_d}(r_{1\alpha}F_{1\beta} + r_{2\beta}F_{2\beta} + r_{3\beta}F_{3\beta} + r_{4\beta}F_{4\beta}) + \\ \frac{1}{4}\sum_{n=1}^{Ni}(r_{1\alpha}F_{1\beta} + r_{2\beta}F_{2\beta} + r_{3\beta}F_{3\beta} + r_{4\beta}F_{4\beta}) \end{array}\right] \tag{3.4}$$

The first term is a kinetic energy of an atom *I* and the second term is a pairwise energy contribution where *n* loops over the N_p neighbors of atom *I*, r_1 and r_2 are the positions of the 2 atoms in the pairwise interaction, and F_1 and F_2 are the forces on the 2 atoms resulting from the pairwise interaction. The third term is a bond contribution of similar form for the N_b bonds which atom I is part of. There are similar terms for the N_a angle, N_d dihedral, and N_i improper interactions atom I is part of.

The components of the stress tensor have the unit of bars.Angstrom^3 and in order to have a unit of pressure, the value will have to be multiplied by the volume occupied by one atom. There is no clear definition of the volume occupied by an atom in a FCC crystal lattice, thus we make an approximation and assign the value $a^3/4$ for the volume occupied by an atom (where a is the lattice constant). As we are only concerned with visualizing how the stress is distributed locally in the np structure, the exact value of the stress per-atom is not significant for the results.

3.2.2 Centrosymmetry Parameter

A centrosymmetric material such as Au, has pairs of equal and opposite bonds for each atom. Kelchner *et al.* made use of this property to characterize defects due to plasticity in centrosymmetric materials. For any homogeneous elastic deformation, centrosymmetric materials remain centrosymmetric. The bonds may get elongated and change direction but they will still have an equal and opposite bond provided that the deformation is elastic. However, in the presence of crystallographic defects, the equal and opposite criteria for bonds are no longer satisfied for nearest neighbor pairs. Kelchner *et al.* [57] defined a centrosymmeteric parameter P that is zero when the elastic deformation does not disrupt the equal and opposite pair of bonds and non-zero when there is plastic deformation:

$$P = \sum_{i=1..6} \left| R_i + R_{i+6} \right|^2 \qquad 3.5$$

where R_i and R_{i+5} are vectors (bonds) corresponding to the six pairs of nearest neighbors for an atom on a FCC lattice. These vectors are calculated for the undistorted FCC lattice of the pristine Au block (without pores). After deformation, the neighbor pairs are located with vectors closest in distance to the undistorted nearest-neighbor vectors in the deformed porous block. Each pair of "equal and opposite" bonds is added together and the sum of the squares of these 6 pairs of bonds is calculated to give the centrosymmetric parameter for atoms in the block.

Kelchner *et al.* [57] have calculated the centrosymmetric parameter for crystalline gold and have shown that this parameter can differentiate between three distinct structures which are atoms that are on the surface, atoms in an intrinsic stacking fault and atoms halfway between an HCP and FCC sites. The centrosymmetric parameter for Au atoms in these environments is shown in Table 1.

Table 1. Centrosymmetric parameter for gold

Types of environments	Centrosymmetric Parameter (Å^2)
Perfect Au lattice	0
Partial dislocation	2.1
Stacking faults	8.3
Surface atoms	24.9

3.3 POSTPROCESSING AND VISUALIZATION

To visualize the np structures, Visual Molecular Dynamics (VMD) software was utilized. The open source software was developed at the University of Urbana-Champaign. The output from the LAMMPS simulation (dump files) for snapshots of the structure during deformation can be visualized by this software and a snapshot of 75% porosity np-Au structure is shown in Figure 5. The VMD software was also used to visualize the von Mises stress states as well as the centrosymmetry parameter values of each atom in the np structures.

Matlab codes were written in order to extract and modify the output of LAMMPS so that VMD software could effectively visualize the von Mises stress state and centrosymmetry parameter for each atom.

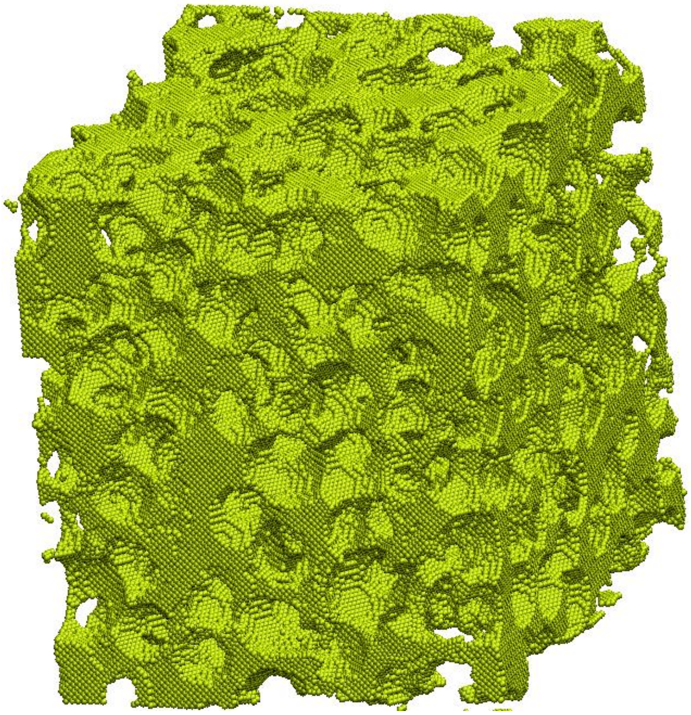

Figure 5: VMD image of 75% porosity np-Au structure.

4.0 RESULTS AND DISCUSSION

4.1 TENSILE RESPONSE OF NANOPOROUS STRUCTURES

The engineering stress-strain relationship of np-Au with different porosities ranging from 66% to 78% under uniaxial tensile loading is shown in Figure 6. The stress rises for the initial elastic region and decreases abruptly thereafter; signifying the brittle nature of np Au. Similar stress-strain relationship was obtained for np-Al in tension which signifies that this behavior can be generalized for np metals. The results of the mechanical properties such as elastic modulus and softening behavior as a function of porosity are shown in Figures 7 and 8. According to Figure 6, the yield stress is reached at 0.5-1.0% strain and the ultimate tensile stress is reached at 3.0-4.0% strain level. The initial linear elastic region allows the calculation of the elastic modulus for all the different porosities by fitting a number of data points in that region to a straight line in the least squares sense.

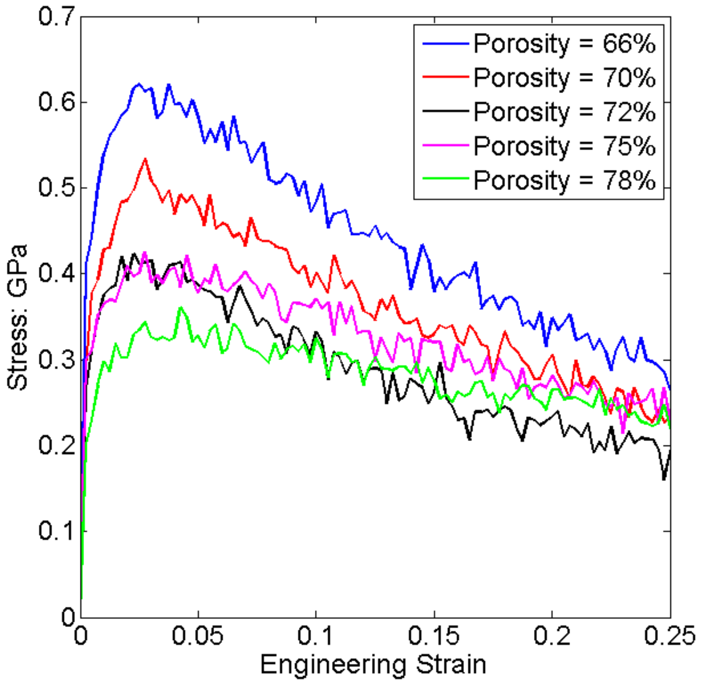

Figure 6: Engineering stress-strain curves for nanoporous Au with different porosities under uniaxial tension.

As discussed earlier, the scaling relationship in Eq. (2.1) establishes a general relation between the Young's modulus to the relative density of open cell porous structures. In the book 'Cellular Solids' [21], the constants in the equations were determined by fitting the plot of experimental values of relative Young's modulus against porosity. We employed the same technique in this work by fitting our simulation results to Eq. (2.1) and obtain the constant C_1. The Young's modulus values for np-Au decrease with increasing porosity which was consistent with the predictions made by Eq (2.1) (Fig. 7). For np-Au the curve fit in Fig. 7 calculated C_1 to be 2.6. The Young's modulus values for np-Au (5-12 GPa) match well with most of the experimentally determined values [9, 27]. To check for ligament and joint size effects on the elastic behavior, np structures with constant porosity but different ligament widths were simulated and their elastic modulus were calculated. The results showed no pronounced effects of microstructural length scale on the Young's modulus of np structures which is consistent with most experimental studies [9, 27].

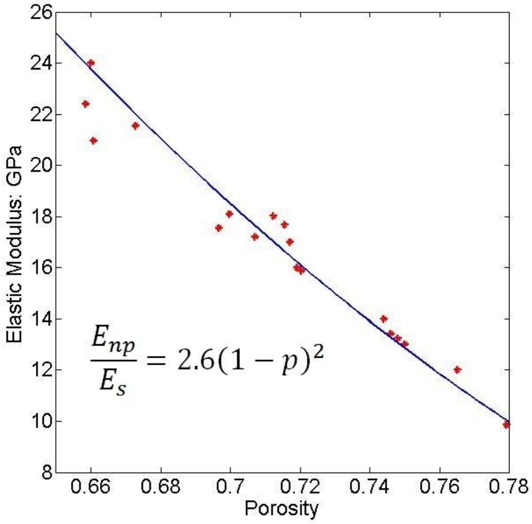

Figure 7: Elastic Modulus vs. Porosity plot for np-Au.

Beyond the elastic region, the stress reaches a peak and abruptly startes to decrease thereafter (Figure 6). All structures tend to soften before they fracture and the rate of softening decreases gradually from 66% to 78% porosity (Figure 8) i.e higher relative density structures soften at a faster rate.

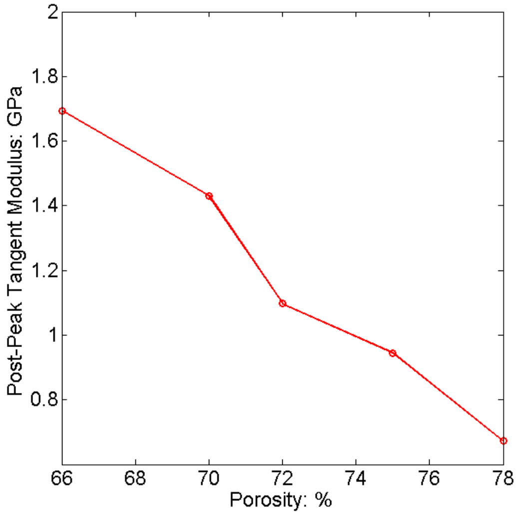

Figure 8: Post peak tangent modulus vs. porosity for np-Au structures.

4.1.1 The influence of ligament and joint size on the softening behavior

As discussed in section (3.1), a random np structure with a specific porosity and pore radius can be approximated by a periodic np structure. Using this approximation, the values of average ligament widths and joint widths for different porosities were computed and shown in Fig. 9. Higher porosity structures have smaller ligament and joint widths while lower porosity structures have thicker ligament and joint widths. For the 78% porosity structures, the ligament size is the smallest and a further increase in porosity would break the interconnected network. The 66% porosity structure had the largest ligament and joint widths and was the smallest porosity possible for an open celled np structure generated using our method.

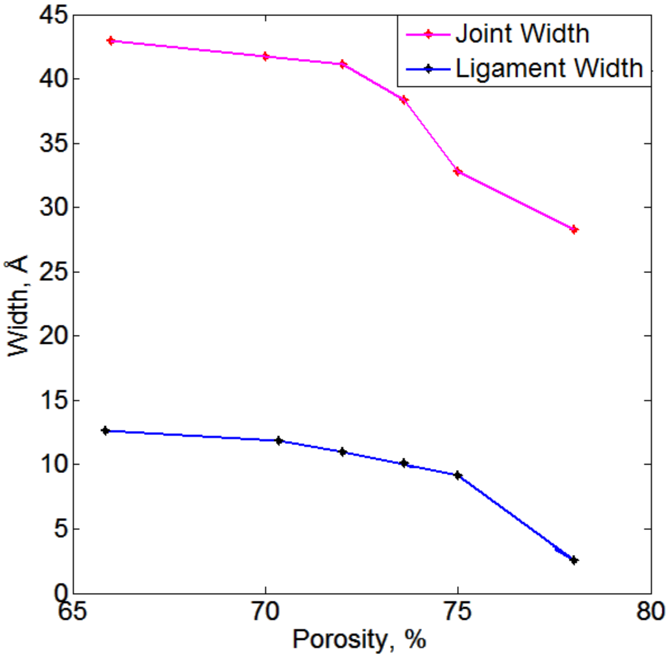

Figure 9: Porosity vs. ligament and joint size plot. Note that ligament size for 78% porosity is very close to zero, which means 78% will be the largest porosity, above which some ligaments will likely break.

To investigate the ligament and joint size influence on the mechanical behavior of the np structures as a whole, we calculated the von Mises stress values for every atom in 70% and 78%

porosities. Note that the ligament and joint width for 66% porosity is larger than that for 78% porosity structures as shown in Fig. 9. The local stress distribution for 70% porosity structure is shown in Figure 10. At 10% strain level, the cracks develop at the regions of stress localization and eventually open up at around 25% strain. For the higher porosity structures (bigger ligament-joint width), stress localizes around the region that was under displacement boundary condition. In contrast, the stress delocalizes over the entire structure for the higher porosity structures. The localization of stress leads to the catastrophic failure of the higher porosity while slower softening occurrs in the higher porosity structure due to delocalization.

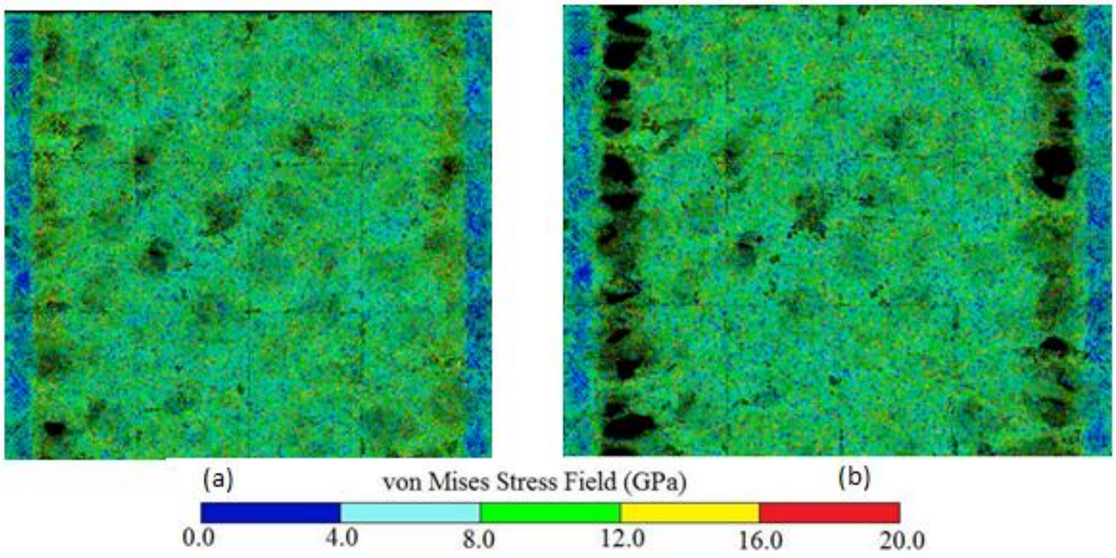

Figure 10: Local von Mises stress distribution for70% porosity np-Au at (a) 10% strain level and (b) 25% strain level.

To show these observations quantitatively, the percentage of atoms that have a particular overall tensile stress level for the 72% and 78% porosity np-Au is shown in Figure 11. The curve for the 72% porosity structure has a heavier right tail. Therefore, the percentage of atoms with

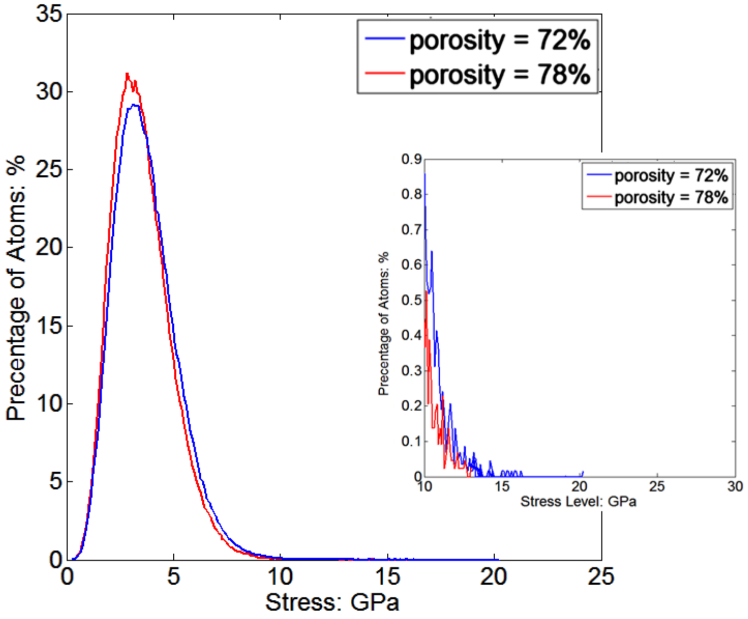

Figure 11: Stress distribution curves at 10% strain for np-Au structures with 72% and 78% porosities.

higher local stresses is larger for the smaller porosity structure. Also, the extreme stress values for the 72% are higher than that for the 78% structures. This proves that larger ligaments and joints experiences higher stress localization which leads to the rupture of the ligaments between the joints and eventually the faster softening of the np structure. For all np-Au structures, ligaments bridging the crack region were observed to be strained by as much as 200%, which is consistent with the SEM images of np-Au samples in Ref. [4].

As mentioned previously, the exact shape and size of the ligaments and joints in the models are very difficult to predict. This is due to the fact that all the spheres are randomly generated in 3D space, thus making the orientation and thickness of the ligaments and joints random as well. From the results of the uniaxial tests performed on np structures, it is evident that ligament and joint sizes influence the softening behavior of these structures. In order to study the basic deformation behavior of a typical ligament connected by a pair of joints, the periodic np structure is employed to generate the single ligament model (see Fig. 5(c)) for uniaxial tension test.

In order to investigate the difference in failure behavior between small and large ligaments, the local von Mises stresses was computed for every atom in the respective models (Fig. 12). Uniaxial tensile test were performed on a small ligament-joint model with 11.83 Å ligament width and 41.29 Å joint width (Fig. 12(a)) and a large ligament-joint model with 9.11 Å ligament width and 29.9 Å joint width (Fig. 12(b)). The comparison between the two ligament-joint models was made at the same stress level. For the larger ligament, stress is mainly localized around the joints (shown as red dot in Fig. 12), while the ligament is under low stress levels. For the small ligament, the entire structure was critically overloaded. This observation points to the fact that stress is distributed more evenly throughout the structure in the smaller ligament-joint model. By examining more ligaments and joints of different sizes, it can be conclude that both the ligament and joint sizes need to be small in order for this observation to hold true. The ligament between two large joints can be thought of as a nanowire with moment resistant boundaries at the two ends. In this context, small ligaments with small joints would have weaker bending resistance than larger ligaments with larger joints. The larger

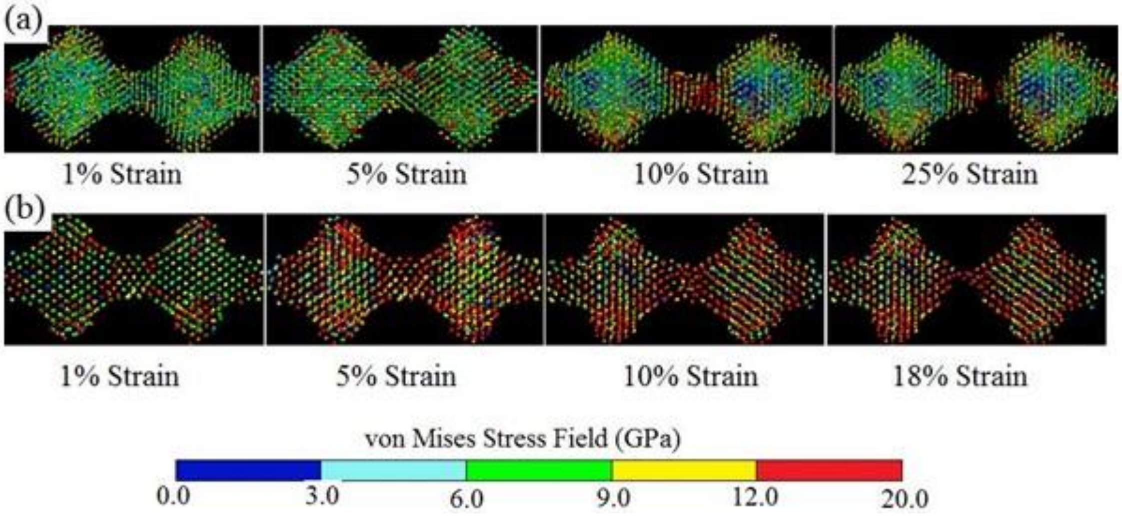

Figure 12: Local von Mises stress plots for ligament-joint models of a) ligament width of 11.83 Å and joint width of 41.29 Å and b) ligament width of 9.11 Å and joint width 29.9 Å at different strain levels.

ligament-joint model resists the external loading better and thus higher localized stresses were observed that lead to catastrophic failure. Aside from this main cause, a secondary reason for the lower softening rate for smaller ligament and joint widths concerns the amount of energy released upon rupture of a ligament. The smaller the ligament, the smaller the amount of energy released upon its rupture for the adjacent ligaments to bear, thus reducing the post peak tangent modulus.

4.2 COMPRESSIVE RESPONSE OF NANOPOROUS STRUCTURES

As mentioned previously, np metals have been shown to behave in a completely different manner in compression compared to when they are loaded in tension. The engineering stress-strain relation of np-Au under uniaxial compression is shown in Figure 13. It is clear that the stress rises abruptly till strain level of ~0.5%. The plots show an indistinct yield point in the range of 50-110 MPa for all porosity structures. The yield strength increases with decreasing

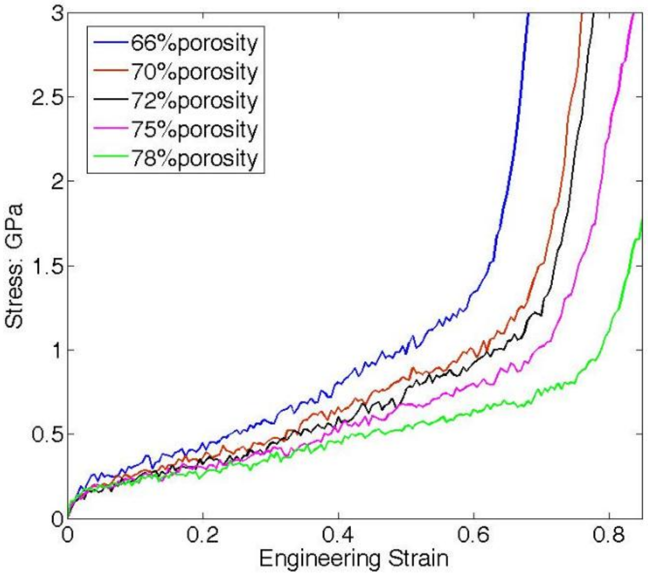

Figure 13: Engineering stress-strain curves for np-Au with different porosities under uniaxial compression.

porosity and the 78% porosity structure has the lowest yield point whereas the 66% porosity structure has the highest value. The approximate yield strength values are higher in tension than in compression as is expected for most materials. After the yield point, considerable strain hardening occurs till a maximum stress is reached. The elastic region for compression is not as distinct as that for uniaxial tension tests, so the Young's modulus values cannot be accurately evaluated. However, a linear fit of the plots in this region did show that the values measured were close to that measured under tensile tests.

Unlike in tension, where stresses localize around ligaments and joints bridging the crack region, stress delocalizes over the entire structure of np-Au under compression. This is observed for all np-Au porosities from 66%-78%. As the compressive strain increases, the stress increases in the structure and delocalizes. Np-Au is very ductile and can be compressed up to ~70% strain level after which the ligaments and joints touch each-other and foam densification occurs.

The scaling relation given by equation (1.3) relates the porosity of the foams to their relative yield strength. In Figure 14, the relative yield strength vs. relative density is plotted for np-Au structures and the curve fit with equation (1.3) for the data points is also included in the figure. The constant C_3 is evaluated to be 4.53 and is higher than the value of 0.3 calculated for

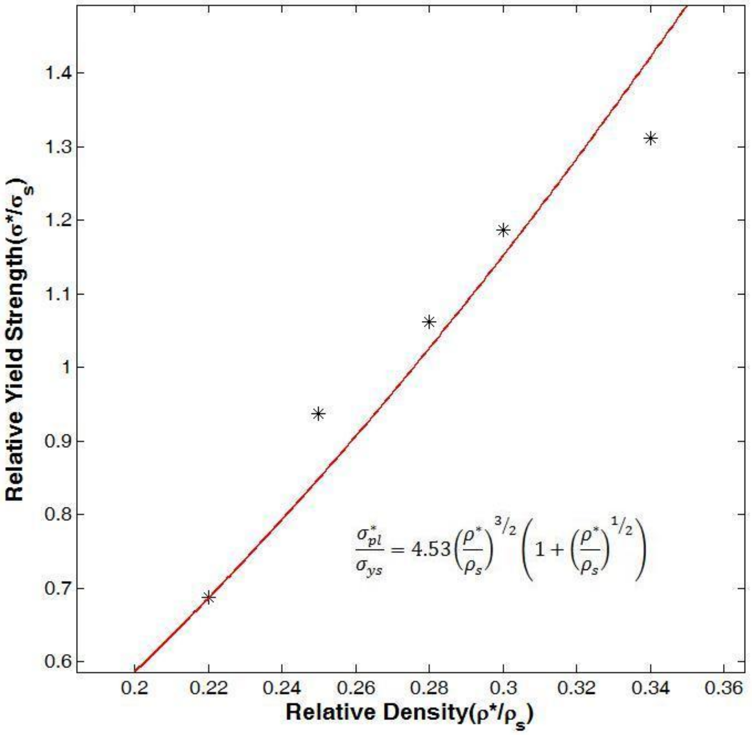

Figure 14: Relative yield strength vs. relative density of np-Au structures.

mp foams. It is important to note that this relationship does not include the length scale effects of the microstructure of np foams and the relatively higher C_3 is a consequence of the influence of the microstructure on the relative yield strength. Whether this constant applies to all np metals with similar morphology is still a subject of concern and beyond the scope of this thesis.

The yield strength of the np-Au structures was found to decrease with decreasing ligament and joint widths, as can be seen from Figures 13 and 14. The ligament and joint width decreases with the decrease in relative density (increase in porosity), but we do not observe the strengthening of np structures with smaller nanostructures as is observed in most experimental studies that have tested ligaments down to 10 nm in size.

Some of the experimental studies have compared the deformation mechanisms involved in Au nanowires to that in np-Au. As mentioned earlier, Ref. [43] state that the mechanisms involved in fcc metallic nanowires such as the reduction in number of defects in grains due to size effects, the repression of emission and reabsorption of dislocations and dislocation nucleation at free surfaces may be the likely mechanisms involved in length scale effects seen in np-Au as well. Greer and Nix [33] showed that the yield strength of submicron Au columns also follow the size dependent characteristics observed in np-Au and that the theoretical yield strength can be achieved when the size of the diameter of Au columns decreases down to a few hundred nanometers.

These size effects have been explained by the presence of free surfaces at the nano-scale that limits the number of dislocation sources. Beiner *et al.* [10] state that the microcolumns of Au can be related to the ligaments in np-Au where the applied stress needed to activate the dislocation sources increases until the theoretical shear strength is reached as the size of the ligaments decreases to 10 nm. Thus, according to them np-Au can be envisioned as a three-dimensional network of defect-free, ultra high strength Au nanowires.

A fundamental difference between the np-Au structures used in experiments and the models simulated in this work is the geometry of the microstructure. The morphology of np-Au in all the experimental studies consists of ligaments and joints that are comparable in size whereas in our models, the joint sizes are an order of magnitude bigger. As stated in Section 1.2.2, the experimental studies have shown that the yield strength can be improved by reducing the ligament size till 10 nm. Their size dependence observed for np-Au is in excellent agreement with the results from microcompression tests on sub-micron Au columns. The higher than expected source activation stress is because of various factors such as changes in active source size, internal stress fields or number of sources. However, size effects due to ligament width less than 10 nm has not been carried out so far. The ligament and joint size in the models presented in this dissertation are well below this minimum ligament size and the “smaller is stronger" relation does not hold for the np-Au structures being simulated. In fact, Diao et al. [58] have shown that for gold nanowires, the compressive yield strength decreases as the nanowire width is decreased below 6 nm. They have attributed this observation on the surface stress driven compression of these nanowires to equilibrium.

To study the plasticity in np-Au, the centrosymmetry parameter (P) [57] was utilized to visualize the defects present in np-Au before and after loading. Figure 16(a) shows a cross-section with a width of 40.8 Å through a 66% porosity structure after energy minimization. Here, the blue atoms corresponds to atoms in a perfect FCC lattice site, the red atoms corresponds to stacking faults (P = 4~20 Å^2), yellow atoms correspond to partial dislocations (P = 0.5~4 Å^2) and white atoms correspond to atoms on the surface (P = 0~0.5 Å^2). Some of the joints have pre-exisisting plastic defects and plastic deformation is induced without any external stress as can be seen in Figure 15(a). The plastic deformation is shown as yellow atoms and this self-induced plasticity is due to the high surface stress values from the ligaments in the np-Au. Figure 16(a) plots the percentage of atoms vs. the centrosymmetric parameter for the initial np-Au structure represented in Figure 16(a). There are high percentages of atoms that are in a perfect Au lattice site which is represented by the highest peak which extends beyond the plot shown. The other peaks denote the percentage of staking faults and surface atoms in the np-Au structure.

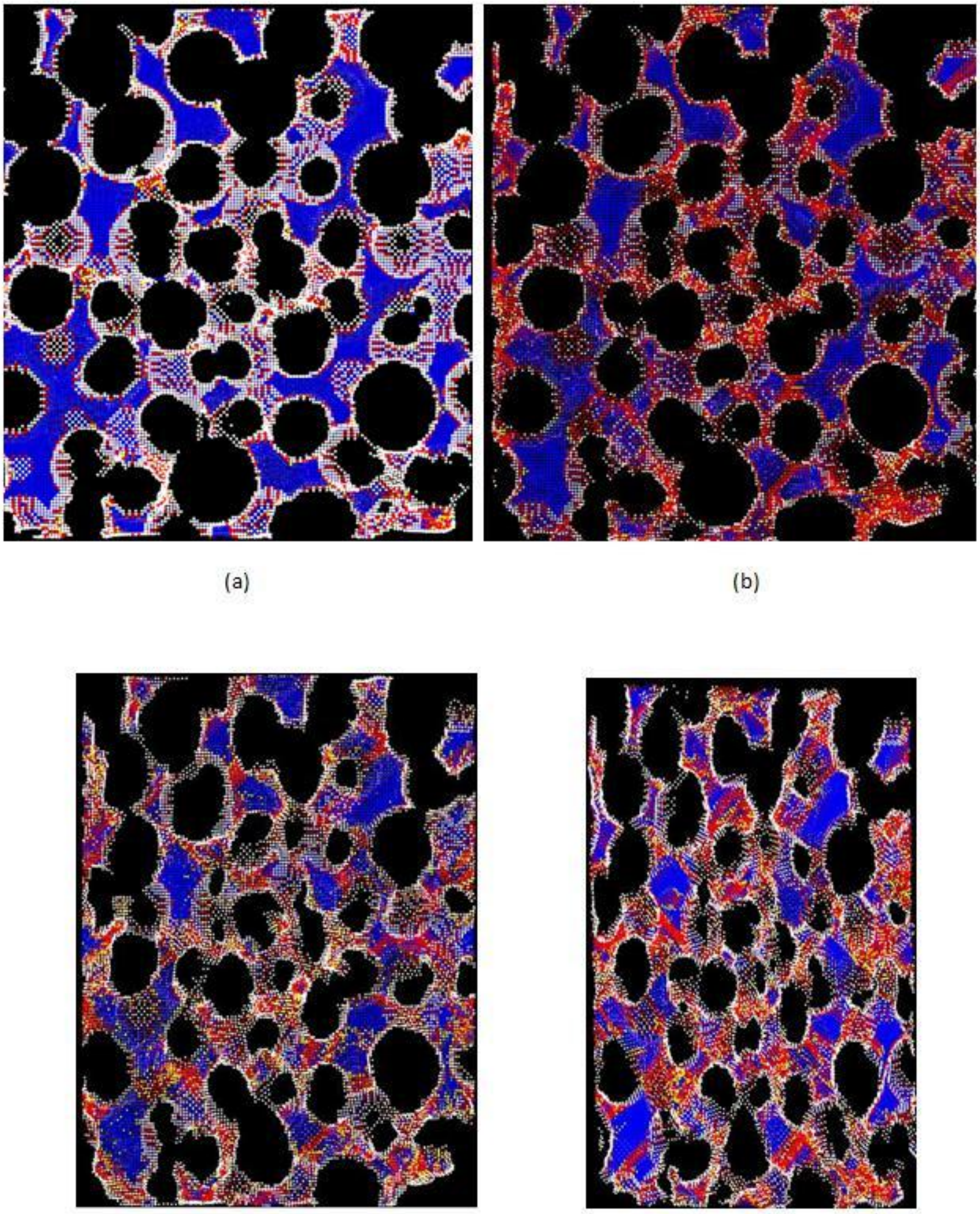

(a) (b)

(c) (d)

Figure 15: Atoms colored according to the Centrosymmetry parameter for a cross-section of np-Au with 66% porosity. (a) Plasticity without any external stress can be seen as red and yellow atoms that cluster up in and around some of the joints after energy minimization. Structures at (b) 10% strain level, (c) 25% strain level and (d) 35% strain level.

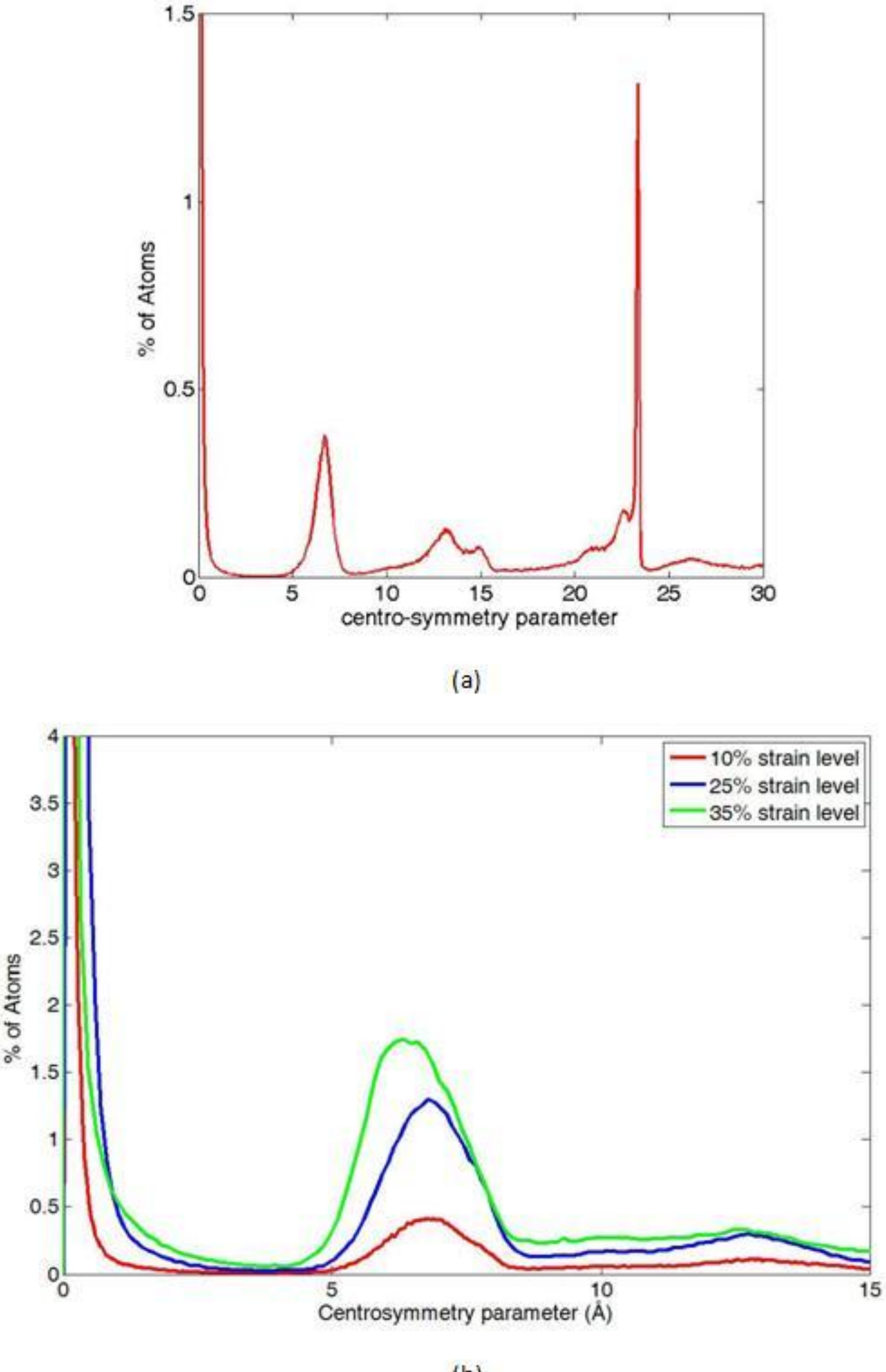

(a)

(b)

Figure 16: Percentage of atoms vs. centrosymmetry parameter for (a) the initial structure without any external stress (peak for surface atoms (P<0.5) rises above 40% of atoms), and (b) the structure at different strain levels.

As the strain is increased, the partial dislocation density increases in the structure as can be seen in Figures 16 and 17. More crystal defects accumulate in and around the joints and partial dislocations pile up. This is shown quantitatively in Figure 16(b) which compares the percentage of atoms with the corresponding centrosymmetric parameter between 66% porosity np-Au at 10%, 25% and 35% strain levels. The percentages of atoms that are in the perfect lattice site at 10% strain are less than the initial structure without external stress (not shown in the plot). The amount of partial dislocations and stacking faults ($0.5\ \text{Å}^2 < P < 20\ \text{Å}^2$) increases for 10% strain level. Beyond the 10% strain level, the crystal defect density increases further and work hardening is observed for all np structures. Work hardening is evident from the stress-strain curves (Figure 13). As the strain increases beyond the linear elastic region, the stress gradually increases to a point after which foam densification is occurs. When a plastic crystal is deformed, dislocations are generated and stored. The storage of dislocations causes the work hardening in the np structures. The localization of partial dislocations in and around the joints is consistent with the work hardening phase seen in this stress-strain relationship and provides visual proof that indeed the storage of dislocations causes the material to work harden.

The work hardening and localization of plastic deformation is consistent with the results from Ref. [27]. Their TEM images of deformed np-Au nanowires also demonstrated the storage of crystal defects near the junctions and nodes of ligaments. Note that their np-Au was in the form of a nanowire. One way to explain this deformation mechanism is by strain gradient hardening mechanism [45] which proposes that there is geometrically necessary dislocations (GND) that are the dislocations generated in the joints which are retained in the structure to account for the gradients of plastic strain. The gradients of plastic strain are usually present in materials due to the geometry of the loading or when the material is plastically inhomogenous.

An example of plastically inhomogeneous material is when a beam is subjected to bending; the strain is zero on the axis of the beam while it is finite on the surface. For the compatible deformation of various parts of the crystal, dislocations are necessary in the structure and this causes the enhanced strengthening of the material. Furthermore, the presence of partial dislocations in the structure is consistent with MD work on gold nanopillars where the partial dislocations propagated along the {111} planes leaving behind a series of stacking faults [59].

Furthermore, the concentration of plastic deformation in and around the joints is also consistent with the deformation mechanism proposed by Gibson and Ashby in which the plastic collapse of the cubic unit cell model occurs due to the deformation of hinges at the nodes. This is caused by the maximum bending moment at these hinges due to the force *F* (Figure 17)

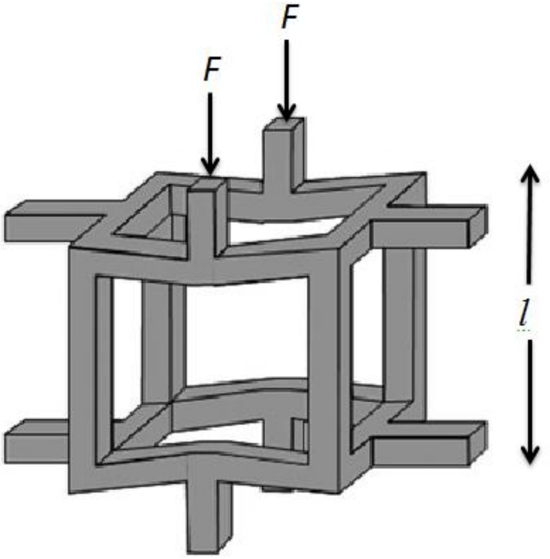

Figure 17: Cell bending of the deformed cubic unit cell.

which exceeds the fully plastic moment of the ligament-joint composites. In the cubic unit cell model of Gibson and Ashby, this moment is given as:

$$M_p = \frac{1}{4}\sigma_{ys}t^3 \tag{3.6}$$

where σ_{ys} is the yield strength of the material that makes up the beams in the unit cell and t is the thickness of each beam. As the thickness of the beam increases, the plastic moment of the unit cell also increases. Thus, thicker beams will be harder to deform plastically by bending. In analogy to the microstructures in the np-Au, the lower porosity structures have larger ligament-joint composites and hence require higher bending moments for plastic deformation. This is consistent with the stress-strain relations for the np-Au structures where 66% porosity structures experience higher stresses under plastic deformation than 78% porosity structures at the same strain level.

5.0 CONCLUSIONS

In this work, we have successfully modeled the complex morphology of np materials which incorporates random cell/pore size, random location of cells in space and non-uniform ligament cross-sections. Through atomistic simulations, the characteristic response of np-Au under uniaxial compressive and tensile loading has been studied. It was found that np-Au is brittle under uniaxial tensile loading and is very ductile under compressive loading. From the engineering stress-strain relationship, it is observed that np-Au have characteristic high yield strength under compression which suggests that these unique materials may even be stronger than bulk Au under compressive forces and also have the advantage of being highly porous.

The macroscopic brittleness of np-Au presents a problem for useful application of these materials but the microstructural features can be tailored to reduce the catastrophic failure of np metals. Using MD simulations, the softening behavior of np-Au structures under tensile loading is observed to slow down significantly when the width of the ligaments and the size of joints become small enough. The relatively compliant ligaments and joints act to spread stress throughout the structure and prevent it from localizing, which would cause slower softening of the np structure.

These materials behave completely different manner under compressive loading compared to tensile loading. Under compression they are very ductile and behave in a characteristic way similar to that of the Gibson and Ashby cubic unit cell model. One important difference between the predicted behavior according to the Gibson and Ashby model and the behavior observed from the atomistic simulations of np-Au is that for the latter there is considerable strain hardening before foam densification occurs. By examining the crystallographic defects, the strain hardening behavior can be attributed to defects in the crystal structure that accumulates at the joints. This observation is consistent with the strain gradient hardening mechanism, which proposes that there are geometrically necessary dislocations to prevent further deformation. Therefore, from the atomistic simulations of np-Au under uniaxial compression, it is evident that the dominant deformation mechanism is bending.

5.1 RECOMMENDATIONS FOR FUTURE WORK

Future work that can be done to further explore the mechanical behavior of np metals are listed below:

- The np structures were that generated for this work have a very uneven size distribution between the small ligaments and the large joints. From Figure 9 it can be seen that the ligament and joint sizes are not comparable. Models that have similar joint and ligament size could be generated by devising a different method for pore creation in the np structure.
- These materials have been used as actuators and their actuation capability comes from varying the magnitude of the surface stress in the ligaments through electrochemical voltage. Different interatomic potential for Au that include surface stress values can be

used to test the mechanical behavior of these materials with different surface stress values in the metal ligaments.

- The method that we have used to probe into the plastic behavior of these materials only distinguishes between three structures as mentioned in Section 3.3. A better way to quantify plasticity in the np structure would explain the deformation mechanism in compression in more detail.
- The simulations involved in this work took very long periods of time due to a large number of atoms simulated. Even at a strain rate of $10^8 s^{-1}$ and large the computational resources provided by the University of Pittsburgh, the simulations took a long period of time. Multiscale methods could be developed to computationally predict the mechanical behavior of these novel materials.
- In this work, the structures being simulated were all single crystal np-Au. However, np-Au formed from dealloying generally is a polygrained structure and the grain boundaries have been shown to influence the mechanical behavior of metals. Polygrained structures could be modeled and tested using MD to study the effect of grain boundaries on the deformation of np materials.
- In experimental studies, it has been reported that dealloyed np-Au from AgAu master alloy contain residual Ag atoms on the grain boundaries. These residual Ag atoms are believed to act as stress concentration sites that ultimately influence the brittle failure of the material in tension. The effect this has on the brittleness could be studied through MD by modeling Ag atoms on the grain boundaries and loading the np structure in tension.
- The effect of temperature on the stress-strain behavior of these materials can be studied to observe how these materials behave quasi-statically as well as in the presence of different

finite temperatures. Also, the effect of temperature on the crystallographic defects can be studied through the method used in this work.

BIBLIOGRAPHY

1. Bonroy, K., et al., *Realization and Characterization of Porous Gold for Increased Protein Coverage on Acoustic Sensors.* Analytical Chemistry, 2004. **76**(15): p. 4299-4306.

2. Erlebacher, J., et al., *Evolution of nanoporosity in dealloying.* Nature, 2001. **410**(6827): p. 450-453.

3. Ganguly, P. and F.-J. Ulm, *Analysis of deformation coupled surface remodeling in porous biomaterials.* Journal of Materials Science, 2007. **42**(21): p. 8873-8884.

4. Kramer, D., R.N. Viswanath, and J. Weissmüller, *Surface-Stress Induced Macroscopic Bending of Nanoporous Gold Cantilevers.* Nano Lett, 2004. **4**(5): p. 793-796.

5. Logar, Z.a.K., V. , *Nanoporous Materials: From Catalysis and Hydrogen Storage to Wastewater Treatment.* Acta Chim. Slov, 2006. **53**.

6. Rösler, J., et al., *Fabrication of nanoporous Ni-based superalloy membranes.* Acta Materialia, 2005. **53**(5): p. 1397-1406.

7. Weissmuller, J., et al., *Charge-induced reversible strain in a metal.* Science, 2003. **300**(5617): p. 312-5.

8. Biener, J., Hamza, A.V. & Hodge, A.M. , *Deformation Behavior of Nanoporous Metals.* Mechanical Engineering, 2007: p. 118-135.

9. Biener, J., et al., *Nanoporous Au: A high yield strength material.* Journal of Applied Physics, 2005. **97**(2): p. 024301.

10. Biener, J., et al., *Size Effects on the Mechanical Behavior of Nanoporous Au.* Nano Lett, 2006. **6**(10): p. 2379-2382.

11. Biener, J., A.M. Hodge, and A.V. Hamza, *Microscopic failure behavior of nanoporous gold.* Applied Physics Letters, 2005. **87**(12): p. 121908.

12. Feng, X.-Q., et al., *Surface effects on the elastic modulus of nanoporous materials.* Applied Physics Letters, 2009. **94**(1): p. 011916.

13. Liu, Z. and P.C. Searson, *Single Nanoporous Gold Nanowire Sensors.* The Journal of Physical Chemistry B, 2006. **110**(9): p. 4318-4322.

14. Ding, Y., Y.J. Kim, and J. Erlebacher, *Nanoporous Gold Leaf: "Ancient Technology"/Advanced Material.* Advanced Materials, 2004. **16**(21): p. 1897-1900.

15. Petegem, S.V., et al., *On the Microstructure of Nanoporous Gold: An X-ray Diffraction Study.* Nano Lett, 2009. **9**(3): p. 1158-1163.

16. Newman, R.C., et al., *Alloy Corrosion*, in *MRS Bulletin*1999. p. 24-28.

17. Li, R. and K. Sieradzki, *Ductile-brittle transition in random porous Au.* Physical Review Letters, 1992. **68**(8): p. 1168-1171.

18. Parida, S., et al., *Volume Change during the Formation of Nanoporous Gold by Dealloying.* Physical Review Letters, 2006. **97**(3): p. 035504.

19. Qian, L.H. and M.W. Chen, *Ultrafine nanoporous gold by low-temperature dealloying and kinetics of nanopore formation.* Applied Physics Letters, 2007. **91**(8): p. 083105-3.

20. Hayes, J.R., et al., *Monolithic nanoporous copper by dealloying Mn–Cu.* Journal of Materials Research, 2006. **21**(10): p. 2611-2616.

21. Gibson L.J. and A. M.F., *Cellular Solids: Structure and Properties*1997: Cambridge University Press.

22. Warren, W.E. and A.M. Kraynik, *The Linear Elastic Properties of Open-Cell Foams.* Journal of Applied Mechanics, 1988. **55**(2): p. 341-346.

23. Zhu, H.X., J.F. Knott, and N.J. Mills, *Analysis of the elastic properties of open-cell foams with tetrakaidecahedral cells.* Journal of the Mechanics and Physics of Solids, 1997. **45**(3): p. 319-343.

24. Durian, D.J., *Bubble-scale model of foam mechanics : Melting , nonlinear behavior , and avalanches.* Physical Review E, 1997. **55(2)**: p. 1739-1751.

25. Xiang, Y., et al., *Mechanical properties of porous and fully dense low-k dielectric thin films measured by means of nanoindentation and the plane-strain bulge test technique.* Journal of Materials Research, 2006(21): p. 386-395.

26. Ko, W.L., *Deformations of Foamed Elastomers.* Journal of Cellular Plastics, 1965. **1**(1): p. 45-50.

27. Dou, R. and B. Derby, *Deformation mechanisms in gold nanowires and nanoporous gold.* Philosophical Magazine, 2011. **91**(7-9): p. 1070-1083.

28. Jin, H.-J., et al., *Deforming nanoporous metal: Role of lattice coherency.* Acta Materialia, 2009. **57**(9): p. 2665-2672.

29. Sun, Y., et al., *In situ indentation of nanoporous gold thin films in the transmission electron microscope.* Microsc Res Tech, 2009. **72**(3): p. 232-41.

30. Volkert, C.A., et al., *Approaching the theoretical strength in nanoporous Au.* Applied Physics Letters, 2006. **89**(6): p. 061920.

31. Xia, R., et al., *Microtensile tests of mechanical properties of nanoporous Au thin films.* Journal of Materials Science, 2009. **44**(17): p. 4728-4733.

32. Legros, M.e.a., *Microsample tensile testing of nanocrystalline metals.* Philos. Mag. A, 2000(80(4)): p. 1017-1026.

33. Greer, J.R. and W.D. Nix, *Size dependence of mechanical properties of gold at the sub-micron scale.* Applied Physics A, 2005. **80**(8): p. 1625-1629.

34. li, R. and K. Sieradzki, *Ductile-Brittle Transition in Random Porous Au.* Physical Review B, 1992. **68**: p. 1168-1171.

35. Shen, T.D., *On the elastic moduli of nanocrystalline Fe, Cu, Ni, and Cu–Ni alloys prepared by mechanical milling/alloying.* Journal of Materials Research, 1998(10(11)): p. 2892-2896.

36. Bauccio, M., ed. *ASM Metals Reference Book*. 3 ed. 1993, ASM, Metals Park.

37. Hodge, A.M., Doucette, R.T., Biener, M.M., Biener, J., Cervantes, O. and Hamza, A.V. , *Ag effects on the elastic modulus values of nanoporous Au foams.* Journal of Materials Research, 2009(24): p. 1600-1606.

38. Mathur, A. and J. Erlebacher, *Size dependence of effective Young's modulus of nanoporous gold.* Applied Physics Letters, 2007. **90**(6): p. 061910.

39. Stafford, C.M., *A buckling-based metrology for measuring the elastic moduli of polymeric thin films.* Nature Materials, 2004(3): p. 545-550.

40. Wu, B., A. Heidelberg, and J.J. Boland, *Mechanical properties of ultrahigh-strength gold nanowires.* Nature Materials, 2005. **4**: p. 525 – 529.

41. Andrews, E.W., et al, *Size effects in ductile cellular solids. Part II: experimental results.* International Journal of Mechanical Sciences, 2001(43(3)): p. 701-713.

42. Hodge, A.M., et al., *Scaling equation for yield strength of nanoporous open-cell foams.* Acta Materialia, 2007. **55**(4): p. 1343-1349.

43. Hakamada, M. and M. Mabuchi, *Mechanical strength of nanoporous gold fabricated by dealloying.* Scripta Materialia, 2007. **56**(11): p. 1003-1006.

44. Horstemeyer M.F., B.M.I., Plimpton S.J., *Length scale and time scale effects on the plastic flow of fcc metals.* Acta Materialia, 2001. **49**: p. 4363-4374.

45. Fleck, N.A., et al., *Strain gradient plasticity: Theory and experiment.* Acta Metallurgica Et Materialia, 1994. **42**(2): p. 475-487.

46. Sun, Y., et al., *The mechanical behavior of nanoporous gold thin films.* JOM Journal of the Minerals, Metals and Materials Society, 2007. **59**(9): p. 54-58.

47. Uchic, M.D., et al., *Sample dimensions influence strength and crystal plasticity*. Science, 2004. **305**(5686): p. 986-9.

48. Balk, T., et al, *Tensile and Compressive Microspecimen Testing of Bulk.* JOM Journal of the Minerals, Metals and Materials Society, 2009. **61**: p. 26-31.

49. Sieradzki, K. and R.C. Newman, *Brittle Behavior of Ductile Metals During Stress-Corrosion Cracking.* Philos. Mag. A, 1992. **51**: p. 95-132.

50. Koh, S.J. and H.P. Lee, *Molecular dynamics simulation of size and strain rate dependent mechanical response of FCC metallic nanowires.* Nanotechnology, 2006. **17**(14): p. 3451-67.

51. Kahng, B., et al., *Electrical breakdown in a fuse network with random, continuously distributed breaking strengths.* Physical Review B, 1988. **37**(13): p. 7625-7637.

52. Chu, T., W. Ranson, and M. Sutton, *Applications of digital-image-correlation techniques to experimental mechanics.* Experimental Mechanics, 1985. **25**(3): p. 232-244.

53. Ercolessi, F. *A molecular dynamics primer*. 1997. **54**, 14.

54. Daw, M.S. and M.I. Baskes, *Embedded-atom method: Derivation and application to impurities, surfaces, and other defects in metals.* Physical Review B, 1984. **29**(12): p. 6443-6453.

55. Kırca, M., et al., *Computational modeling of micro-cellular carbon foams.* Finite Elements in Analysis and Design, 2007. **44**(1–2): p. 45-52.

56. FrantzDale, B., S.J. Plimpton, and M.S. Shephard, *Software components for parallel multiscale simulation: an example with LAMMPS.* Eng. with Comput., 2010. **26**(2): p. 205-211.

57. Kelchner, C.L., S.J. Plimpton, and J.C. Hamilton, *Dislocation nucleation and defect structure during surface indentation.* Physical Review B, 1998. **58**(17): p. 11085-11088.

58. Diao, J., et al., *Atomistic simulations of the yielding of gold nanowires.* Acta Materialia, 2006. **54**(3): p. 643-653.

59. Zepeda-Ruiz, L.A., et al., *Mechanical response of freestanding Au nanopillars under compression.* Applied Physics Letters, 2007. **91**(10): p. 101907.